REPORT DOCUMENTATION PAGE	Form Approved OMB NO. 0704-0188

1. REPORT DATE (DD-MM-YYYY) 18-04-2022	2. REPORT TYPE Final Report	3. DATES COVERED (From - To) 1-Feb-2019 - 31-May-2022

4. TITLE AND SUBTITLE Final Report: Parametrized Model Order Reduction for Engineered Coastal and Hydraulic Systems: Component Libraries and Digital Twins	5a. CONTRACT NUMBER W911NF-19-1-0098
	5b. GRANT NUMBER
	5c. PROGRAM ELEMENT NUMBER 611102
6. AUTHORS	5d. PROJECT NUMBER
	5e. TASK NUMBER
	5f. WORK UNIT NUMBER

7. PERFORMING ORGANIZATION NAMES AND ADDRESSES Massachusetts Institute of Technology (MIT 77 Massachusetts Avenue NE18-901 Cambridge, MA 02139 -4307	8. PERFORMING ORGANIZATION REPORT NUMBER
9. SPONSORING/MONITORING AGENCY NAME(S) AND ADDRESS (ES) U.S. Army Research Office P.O. Box 12211 Research Triangle Park, NC 27709-2211	10. SPONSOR/MONITOR'S ACRONYM(S) ARO 11. SPONSOR/MONITOR'S REPORT NUMBER(S) 74702-MA.1

12. DISTRIBUTION AVAILIBILITY STATEMENT

Approved for public release; distribution is unlimited.

13. SUPPLEMENTARY NOTES

The views, opinions and/or findings contained in this report are those of the author(s) and should not contrued as an official Department of the Army position, policy or decision, unless so designated by other documentation.

14. ABSTRACT

15. SUBJECT TERMS

16. SECURITY CLASSIFICATION OF:			17. LIMITATION OF ABSTRACT	15. NUMBER OF PAGES	19a. NAME OF RESPONSIBLE PERSON
a. REPORT	b. ABSTRACT	c. THIS PAGE			Anthony Patera
UU	UU	UU	UU		19b. TELEPHONE NUMBER 617-253-8122

Standard Form 298 (Rev 8/98)
Prescribed by ANSI Std. Z39.18

RPPR Final Report
as of 21-Apr-2022

Agency Code: 21XD

Proposal Number: 74702MA **Agreement Number: W911NF-19-1-0098**

INVESTIGATOR(S):

Name: Anthony T Patera
Email: patera@mit.edu
Phone Number: 6172538122
Principal: Y

Organization: **Massachusetts Institute of Technology (MIT)**
Address: 77 Massachusetts Avenue, Cambridge, MA 021394307
Country: USA
DUNS Number: 001425594 EIN: 042103594

Report Date: 14-May-2022 Date Received: 18-Apr-2022
Final Report for Period Beginning 01-Feb-2019 and Ending 31-May-2022
Title: Parametrized Model Order Reduction for Engineered Coastal and Hydraulic Systems: Component Libraries and Digital Twins
Begin Performance Period: 01-Feb-2019 **End Performance Period:** 31-May-2022
Report Term: 0-Other
Submitted By: Anthony Patera Email: patera@mit.edu
Phone: (617) 253-8122
Distribution Statement: 1-Approved for public release; distribution is unlimited.

STEM Degrees: 0 **STEM Participants:**

Major Goals: Statement of Objectives. We plan to develop a port-reduced reduced-basis component (PR-RBC) approach for the partial differential equations (PDEs) which govern flow in riverine and coastal environments, with particular emphasis on the Navier-Stokes equations. The methods can be applied in two contexts: the analysis of a new hydraulic system synthesized from a library of generic parametrized components; the analysis of a monitored hydraulic system represented as a digital twin. In both cases the quantities of interest are flowrates and hydrodynamic forces. We shall also consider a passive scalar, such as temperature or contaminant.

Methods to be Employed. The PR-RBC method incorporates several principal ingredients: component-to-system model construction, underlying ``truth'' finite element PDE discretization, (Petrov)-Galerkin projection, parametrized model-order reduction for both the inter-component (port) and intra-component (bubble) degrees of freedom, POD and Greedy training methods for both the port and bubble reduced spaces, offline-online computational decompositions, and parallel implementations. In this work the PR-RBC formulation is expanded to treat nonlinear elliptic partial differential equations; future work will consider hybrid finite element + PR-RBC approaches for problems characterized by advancing fronts or (local) complex coupled phenomena such as Fluid-Structure Interaction.

Significance of Proposed Activity. The PR-RBC approach can yield computational savings of one or two orders of magnitude in both the ``library'' and ``digital twin'' frameworks. Riverine flows constitute an important application relevant in many ARO-related contexts, but more generally serve as an ambitious goal by which to motivate, develop, and assess the PR-RBC approach for nonlinear problems. The underlying technical challenges are fundamental --- related to approximation theory, error estimation, and computational methodology --- and the range of problems and disciplines to which the resulting PR-RBC techniques can be applied is very broad.

Collaboration: This project has benefited from discussions with Dr Chris Kees.

Accomplishments: There are three main computational challenges in this project: extension of PR-RBC to (i) nonlinear problems, (ii) incompressibility constraints, and (iii) convection-dominated elliptic PDEs. As regards (i), we replaced static condensation --- efficient, but no longer relevant in the nonlinear context --- with bubble spaces which are now associated with port spaces rather than individual port modes. As regards (ii), we developed a representation for the flow field in terms of a unity-flowrate function plus a complete set of zero-flowrate functions; the latter play an important role, for example, in the port training procedure. As regards (iii) (for a passive scalar model problem), we replaced (downstream) Dirichlet conditions in the training stage --- both for port and bubble subproblems --- with homogeneous Neumann conditions; the latter eliminates artificial downstream boundary layers, which in turn greatly reduces offline and online computational effort.

We have demonstrated the technique on a flow problem with passive scalar in a 2-D riverine geometry (with islands).

Finally, we have completed and submitted a comprehensive journal article which addresses all aspects of the research, from formulation and methodology to computational considerations and implementation to theory and numerical tests to applications.

Training Opportunities: Nothing to Report

Results Dissemination: Nothing to Report

Honors and Awards: Nothing to Report

Protocol Activity Status:

Technology Transfer: We filed an invention disclosure form, Nonlinear Port-Reduced Reduced Basis Component, Case No. 24180, to the MIT Technology Licensing Office.

PARTICIPANTS:

Participant Type: PD/PI
Participant: Anthony Patera
Person Months Worked: 1.00 **Funding Support:**
Project Contribution:
National Academy Member: N

Participant Type: Postdoctoral (scholar, fellow or other postdoctoral position)
Participant: Amina Benaceur
Person Months Worked: 4.00 **Funding Support:**
Project Contribution:
National Academy Member: N

International Travel:

MAR	28 days

Partners

,

I certify that the information in the report is complete and accurate:
Signature: atp
Signature Date: 4/18/22 5:08PM

Final Report for ARO Grant Number W911NF1910098

Grant Title: Parametrized Model Order Reduction for Engineered Coastal and Hydraulic Systems: Component Libraries and Digital Twins

Principal Investigator

Anthony T Patera

Institution

Massachusetts Institute of Technology

April 1, 2022

This document (preprint) has also been submitted to the journal AMSES, Advanced Modeling and Simulation in Engineering Sciences, on March 21, 2022.

RESEARCH

Port-Reduced Reduced-Basis Component Method for Steady State Navier–Stokes and Passive Scalar Equations

Amina Benaceur[*] and Anthony T. Patera[*]

[*] Correspondence:
benaceur@mit.edu;
patera@mit.edu
Department of Mechanical Engineering, Massachusetts Institute of Technology, Cambridge, USA
Full list of author information is available at the end of the article

Abstract

We develop a Port-Reduced Reduced-Basis Component approach (PR-RBC) to solve partial differential equations (PDEs) that govern incompressible fluid flows in riverine geometries. The PR-RBC method was initially introduced in the literature for linear problems. In this paper, we extend it to a nonlinear context. Our method is presented for the steady state Navier–Stokes problem with an incompressibility constraint. The model is supplemented with a passive scalar equation. We introduce a new method for the treatment of nonlinearity, incompressibility, and convective effects.

Keywords: Nonlinear model reduction; Port-reduced reduced-basis component approach; Navier-Stokes equation; Passive scalar equation; Reduced basis

1 Introduction

Riverine and nearshore hydrodynamic conditions are important for a wide variety of engineering applications. In these applications, model accuracy can be critical for cost and human safety considerations, but the timeliness of predictions is just as crucial: the time required to set up, run, and post-process high-fidelity models of riverine hydraulic processes continues to be a major barrier to their application in various contexts. Indeed, as a result of the large time-to-solution associated with high-fidelity models, low-fidelity models with automated workflows are necessary in most cases. Moreover, hydraulic systems usually have repeating geometric patterns that form the global structure. Thus, a framework for the construction of low-fidelity models of large riverine systems from sub-components is very appealing, particularly when the resulting models are characterized by significant improvements in computational and human efficiency relative to the time-intensive high-fidelity components from which the system models are synthesized.

One popular approach for component-based model reduction is the Port-Reduced Reduced Basis Component (PR-RBC) method [1]. The PR-RBC method incorporates aspects of the Component Mode Synthesis (CMS) technique [2, 3, 4] and the Reduced Basis (RB) method [5, 6, 7]. The former contributes components and associated port-bubble approximation; the latter introduces the framework for systematic parametric analysis. The Reduced Basis Element (RBE) method [8] represents the first synthesis of the CMS and RB approaches. The PR-RBC method may thus be viewed as an RBE method for a particular (Static Condensation [9]) choice for the interface treatment and particular strategies for port [10, 11, 12, 13] and bubble [14, 15] approximation spaces. The PR-RBC method comprises several principal ingredients: component-to-system model construction; underlying 'truth' Finite Element (FE) PDE discretization; (Petrov)-Galerkin projection parametrized model-order reduction for both the inter-component (port) and intra-component (bubble) degrees of freedom; offline-online computational decompositions; and parallel implementations. Introduced in the linear case, the PR-RBC method can be applied in two frameworks: (i) the analysis of a new (e.g., hydraulic) system synthesized from a library of archetype parametrized components associated with some large family of problems (e.g., riverine flows), and (ii) the analysis of a particular monitored, deployed, or existing system represented as a slowly evolving digital twin. In the context of elliptic PDEs, the PR-RBC approach can yield computational savings of one or two orders of magnitude in both the 'library' [16] and 'digital twin' frameworks.

In this paper we expand the capabilities of the PR-RBC approach in three directions. First, we consider an incompressibility constraint which introduces additional (and global) coupling between components. Second, we consider nonlinearity, in particular the (incompressible) Navier-Stokes equations. We shall pursue standard Galerkin approximation, not the EIM approach [17], in order to focus on the essential innovation: the standard PR-RBC approach of static condensation can not be applied since superposition is no longer valid. Third, we consider convectively-dominated flows: the evanescence property — which reduces coupling between components — is now quite weak, and different training procedures must be considered. We shall study the effect of strong convection in the context of a passive scalar: the Reynolds number for Navier-Stokes shall remain smaller to avoid (here) extraneous issues related to outflow stability; the Peclet number for the passive scalar equation shall be increased to represent the dominant convective effects.

Model reduction has been addressed for convection dominated problems, e.g., in [18] and [19], and in the absence of components for the Navier-Stokes equation, e.g., in [20] and [21]. It has also been addressed using domain decomposition as in [22] and [23]. Unlike domain decomposition based techniques, the major advantage of the PR-RBC approach is exploiting repeating patterns to define a library of components. This idea factorizes the offline stage and allows for the reconstruction of a large set of geometries using the library components online.

The remainder of this paper is organized as follows. Section 2 introduces the notation that will be used and the model problem that will be addressed in this paper. In Section 3, we extend the PR-RBC to the steady Navier-Stokes problem supplemented with a passive scalar equation. Section 4 presents numerical results illustrating the performance of the nonlinear PR-RBC for two cases of two-dimensional non-forked riverine (or channel) geometries, including a Seine-like configuration.

2 Preliminaries

In this section, we set the notation that will be used throughout the paper. Then, we present our model problem and the Finite Element (FE) [24, 25] solution strategy in a component-based framework and in a two-dimensional setting. The methodology we propose can be extended to three-dimensional problems. We highlight that our method is only applicable to the case of non-forked riverine geometries; forked geometries will need additional development.

We consider a spatial open bounded domain $\Omega \subset \mathbb{R}^2$ with boundary $\partial\Omega$, and a partition of the boundary $\partial\Omega := \partial\Omega^{\text{in}} \cup \partial\Omega^{\text{out}} \cup \partial\Omega^{\text{wall}} \cup \partial\Omega^{\text{cavity}}$. We further define the Hilbert spaces $\mathcal{X} := [H^1(\Omega)]^2$, $\mathcal{Y} := H^1(\Omega)$, $\mathcal{Z} := \{\theta \in \mathcal{Y} \mid v_{|\partial\Omega^{\text{in}}} = 0\}$, and $\mathcal{Q} := \{q \in L^2(\Omega) \mid \int_\Omega q = 0\}$, where $L^2(\Omega)$ is the space of square integrable functions over Ω and $v \in H^1(\Omega)$ means that v and its partial derivatives are all in $L^2(\Omega)$. For further use, $H^1_0(\Omega)$ is the subspace of $H^1(\Omega)$ with vanishing values at the boundaries of Ω. The elements of $\mathcal{X}$ are vectors that will be denoted $v := (v_1, v_2)$. We endow $\mathcal{X}$ with the inner product $(v, w)_{\mathcal{X}} := \int_\Omega C_{\mathcal{X}} \nabla v \cdot \nabla w + \int_\Omega vw$ and we endow $\mathcal{Y}$ with the inner product $(\theta, \tau)_{\mathcal{Y}} := \int_\Omega C_{\mathcal{Y}} \nabla\theta \cdot \nabla\tau + \int_\Omega \theta\tau$, where $C_{\mathcal{X}}$ and $C_{\mathcal{Y}}$ are dimensionality homogenization constants. The induced norms are $\|v\|_{\mathcal{X}} := \sqrt{(v, v)_{\mathcal{X}}}$ and $\|\theta\|_{\mathcal{Y}} := \sqrt{(\theta, \theta)_{\mathcal{Y}}}$, respectively. We consider a compact parameter set $\mathcal{P} = \mathcal{P}_{\text{Re}} \times \mathcal{P}_{\text{Pr}} \subset (\mathbb{R}^*)^2$, where the superscript $*$ indicates the exclusion of the zero element; the elements in $\mathcal{P}$ will be denoted (μ, η). In our setting, $\mu \in \mathcal{P}_{\text{Re}}$ is a Reynolds number and $\eta \in \mathcal{P}_{\text{Pr}}$ is a Prandtl number.

For given parameter values $\mu \in \mathcal{P}_{\text{Re}}$ and $\eta \in \mathcal{P}_{\text{Pr}}$, we introduce the parametrized continuous bilinear forms $a_l(\mu; \cdot, \cdot) : \mathcal{X} \times \mathcal{X} \to \mathbb{R}$ and $d(\mu, \eta; \cdot, \cdot) : \mathcal{Y} \times \mathcal{Y} \to \mathbb{R}$, a continuous bilinear form $b : \mathcal{Q} \times \mathcal{X} \to \mathbb{R}$ and a trilinear form $a_{nl} : \mathcal{X} \times \mathcal{X} \times \mathcal{X} \to \mathbb{R}$ defined by

$$a_l(\mu; v, w) = \frac{1}{\mu} \int_\Omega \nabla v \cdot \nabla w, \qquad d(\mu, \eta; T, \theta) = \frac{1}{\mu\eta} \int_\Omega \nabla T \cdot \nabla\theta, \qquad b(q, v) = \int_\Omega \nabla q \cdot v, \tag{1}$$

$$a_{nl}(u, v, w) = \int_\Omega (u \cdot \nabla v) w. \tag{2}$$

Finally, for $v \in \mathcal{X}$, we introduce the parametrized continuous bilinear form $c(v) : \mathcal{Y} \times \mathcal{Y} \to \mathbb{R}$

$$c(v)(T, \theta) = \int_\Omega (\nabla T \cdot v)\theta. \tag{3}$$

2.1 Model Problem

We address an incompressible steady state Navier–Stokes equation that governs a fluid flow in a riverine geometry. We supplement the Navier–Stokes equation with a passive scalar equation for (say) temperature. Under the hypotheses of a fixed geometry and a non convection-dominated problem (i.e., for a relatively small Reynolds number μ), we search for the solution field $(u(\mu), p(\mu)) \in$

$\mathcal{X} \times \mathcal{Q}$ satisfying the system

$$\begin{aligned} a_l(\mu; u(\mu), v) + a_{nl}(u(\mu), u(\mu), v) - b(p(\mu), v) &= 0, && \forall v \in [H_0^1(\Omega)]^2, && \text{(4a)} \\ b(q, u(\mu)) &= 0, && \forall q \in \mathcal{Q}, && \text{(4b)} \\ u(\mu) &= \bar{u}, && \text{on } \partial\Omega^{\text{in}} \cup \partial\Omega^{\text{out}}, && \text{(4c)} \\ u(\mu) &= 0, && \text{on } \partial\Omega^{\text{wall}} \cup \partial\Omega^{\text{cavity}}. && \text{(4d)} \end{aligned}$$

By virtue of nondimensionalisation, we take $\bar{u}$ to be a unity-flowrate parabola applied at both the inflow and outflow boundaries of the system, i.e., $\int_{\partial\Omega^{\text{in}}} \bar{u} = \int_{\partial\Omega^{\text{out}}} \bar{u} = 1$; note that the unity-flowrate boundary conditions are compatible with the incompressibility condition (4b). In the present setting, we set the velocity field $u(\mu)$ to be the variable of interest. The pressure field $p(\mu)$ can be retrieved using pressure recovery techniques [26]. We also search for the temperature field $T(\mu, \eta) \in \mathcal{Y}$ satisfying the system

$$\begin{aligned} c(u(\mu))(T, \theta) + d(\mu, \eta; T, \theta) &= 0, && \forall \theta \in \mathcal{Z}, && \text{(5a)} \\ T(\mu, \eta) &= 1, && \text{on } \partial\Omega^{\text{in}}, && \text{(5b)} \\ T(\mu, \eta) &= 0, && \text{on } \partial\Omega^{\text{cavity}}, && \text{(5c)} \\ \frac{\partial}{\partial n}(T(\mu, \eta)) &= 0, && \text{on } \partial\Omega^{\text{out}} \cup \partial\Omega^{\text{wall}}. && \text{(5d)} \end{aligned}$$

Note that we use homogeneous Neumann boundary conditions at system outflow given our interest in dominant convective effects (large $\mu\eta \equiv$ Peclet number). We refer the reader to [27, 28] for the wellposedness of (4) and to [29] for the wellposedness of (5).

2.2 Component-Based System

Consider a decomposition of the domain Ω into M subdomains, with $M \in \mathbb{N}^*$. In other words, $\bar{\Omega} := \cup_{i=1}^{M} \bar{\Omega}_i$. For $i \neq j \in \{1, \ldots, M\}$, the non-empty intersections of $\bar{\Omega}_i$ and $\bar{\Omega}_j$ shall be referred to as ports, and they will be denoted Γ_j, with $j \in \{2, \ldots, M\}$. The inflow and outflow boundaries of the system will be denoted Γ_1 and Γ_{M+1} respectively, i.e., $\Gamma_1 = \partial\Omega^{\text{in}}$ and $\Gamma_{M+1} = \partial\Omega^{\text{out}}$. We make the following assumptions:

(a) The subdomains can only be chosen from a library of archetype components defined on the reference domains $\hat{\Omega}_1, \ldots, \hat{\Omega}_{n_c}$, where $n_c \in \mathbb{N}^*$ is the cardinality of the library of archetype components. The occurrences of these archetype components in a new system are referred to as instantiations.

(b) The ports are mutually disjoint.

(c) Each instantiated archetype component has two ports.

Thus, each instantiated archetype component defined on a subdomain Ω_i is linked to the rest of the geometry through the ports Γ_i and Γ_{i+1}. It follows from assumption (a) that the ports can all be mapped to a set of archetype ports $\hat{\Gamma}_1, \ldots, \hat{\Gamma}_{n_p}$, where $n_p \in \mathbb{N}^*$ is the number of archetype ports.

Figure 1: Port/bubble decomposition of Ω in a simplified two-dimensional setting. The inner boundary of Ω_2 is $\partial\Omega^{\text{cavity}}$.

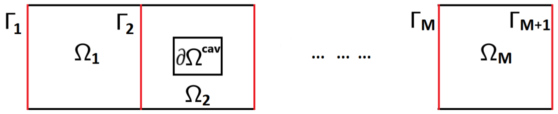

We highlight that these assumptions are well justified in riverine contexts. Our method focuses on non-forked riverine geometries, i.e., geometries without diverging branches; any branches will be handled within the same component. Figure 1 illustrates the introduced component-based domain decomposition in a simplified two-dimensional setting. Note we shall discuss later the translation-rotation mappings which will serve to instantiate archetype components.

For future developments, we define unity-flowrate parabolas $\{\bar{u}_j\}_{1\leqslant j\leqslant M+1}$ on the ports $\{\Gamma_j\}_{1\leqslant j\leqslant M+1}$. We also introduce the linear 'bubble spaces'

$$\mathcal{X}_i^b := \{v \in \mathcal{X} |\ v_{|\Omega\backslash\Omega_i} = 0,\ v_{|\Gamma_i} = 0,\ v_{|\Gamma_{i+1}} = 0,\ div(v) = 0\}, \tag{6}$$

$$\mathcal{Y}_i^b := \{\theta \in \mathcal{Y} |\ \theta_{|\Omega\backslash\Omega_i} = 0,\ \theta_{|\Gamma_i} = 0,\ \theta_{|\Gamma_{i+1}} = 0\}, \tag{7}$$

and the linear 'port spaces'

$$\mathcal{X}_i^p := \{v \in [H^{\frac{1}{2}}(\Gamma_i)]^2,\ \int_{\Gamma_i} v_1 = 1\}, \tag{8}$$

$$\mathcal{Y}_i^p := \{\theta \in H^{\frac{1}{2}}(\Gamma_i)\}. \tag{9}$$

The idea of the PR-RBC initially introduced in [10] is to search for solution fields that are the sum of port and bubble contributions. In order to account for the incompressibility condition in (4b), for every $i \in \{1, \ldots, M\}$, we introduce a constant local contribution $\bar{\bar{u}}_i$ defined on Ω_i as the solution of the following Stokes problem

$$a_l(1; \bar{\bar{u}}_i, v) - b(p, v) = 0, \qquad \forall v \in \mathcal{X}_i, \tag{10a}$$

$$b(q, \bar{\bar{u}}_i) = 0, \qquad \forall q \in \mathcal{Q}_i, \tag{10b}$$

$$\bar{\bar{u}}_i = \bar{u}_i, \qquad \text{on } \Gamma_i, \tag{10c}$$

$$\bar{\bar{u}}_{i+1} = \bar{u}_{i+1}, \qquad \text{on } \Gamma_{i+1}, \tag{10d}$$

$$\bar{\bar{u}}_i = 0, \qquad \text{on } \partial\Omega_i\backslash(\Gamma_i \cup \Gamma_{i+1},), \tag{10e}$$

where $\mathcal{X}_i$ and $\mathcal{Q}_i$ are defined on the subdomain Ω_i in the same fashion as $\mathcal{X}$ and $\mathcal{Q}$ are defined on Ω. We can then define the global constant contribution $\bar{\bar{u}} \in \mathcal{X}$ such that

$$\bar{\bar{u}} = \bar{\bar{u}}_i, \qquad \text{in } \Omega_i, \quad \forall i \in \{1, \dots, M\}, \tag{11}$$

$$\bar{\bar{u}} = \bar{u}_i, \qquad \text{on } \Gamma_i, \quad \forall i \in \{2, \dots, M\}. \tag{12}$$

Using velocity lifting operators $\mathcal{L}^p_{i,u} : \mathcal{X}^p_i \to \mathcal{X}$ and $\mathcal{L}^b_{i,u} : \mathcal{X}^b_i \to \mathcal{X}$, we search for a solution to (4) under the form

$$u(\mu) = \bar{\bar{u}} + \sum_{i=2}^{M} \mathcal{L}^p_{i,u} u^p_i(\mu) + \sum_{i=1}^{M} \mathcal{L}^b_{i,u} u^b_i(\mu), \tag{13}$$

where $u^p_i(\mu) \in \mathcal{X}^p_i$ is a velocity port contribution and $u^b_i(\mu) \in \mathcal{X}^b_i$ is a velocity bubble contribution. Note that the system inflow port Γ_1, the system outflow port Γ_{M+1}, and the incompressibility condition are all handled by $\bar{\bar{u}}$. Thus, $u(\mu) - \bar{\bar{u}}$ is a divergence-free field.

Similarly, we account for the temperature Dirichlet boundary condition (5b) by introducing a lifting $T_{\text{dir},1} \in \mathcal{Y}_1$ that satisfies

$$\int_\Omega \nabla T_{\text{dir},1} \cdot \nabla \theta = 0, \qquad \forall \theta \in \mathcal{Z}_1, \tag{14a}$$

$$T_{\text{dir},1} = 1, \qquad \text{on } \Gamma_1, \tag{14b}$$

$$T_{\text{dir},1} = 0, \qquad \text{on } \Gamma_2 \cup \partial\Omega^{\text{cav}}_1, \tag{14c}$$

$$\frac{\partial T_{\text{dir},1}}{\partial n} = 0, \qquad \text{on } \partial\Omega^{\text{wall}}_1, \tag{14d}$$

where $\mathcal{Y}_1$, $\mathcal{Z}_1$, $\partial\Omega^{\text{cav}}_1$, and $\partial\Omega^{\text{wall}}_1$ are defined on the subdomain Ω_1 in the same fashion as $\mathcal{Y}$, $\mathcal{Z}$, $\partial\Omega^{\text{cavity}}$, and $\partial\Omega^{\text{wall}}$ are defined on Ω. Thus, the global Dirichlet lifting $T_{\text{dir}} \in \mathcal{Y}$ is defined as

$$T_{\text{dir}} := \begin{cases} T_{\text{dir},1} & \text{on } \Omega_1, \\ 0 & \text{on } \Omega \backslash \Omega_1. \end{cases} \tag{15}$$

We search for a solution to (5) under the form

$$T(\mu, \eta) = T_{\text{dir}} + \sum_{i=2}^{M+1} \mathcal{L}^p_{i,T} T^p_i(\mu, \eta) + \sum_{i=1}^{M} \mathcal{L}^b_{i,T} T^b_i(\mu, \eta), \tag{16}$$

where $T^p_i(\mu, \eta) \in \mathcal{Y}^p_i$ is a temperature port contribution, $T^b_i(\mu, \eta) \in \mathcal{Y}^b_i$ is a temperature bubble contribution and $\mathcal{L}^p_{i,u} : \mathcal{Y}^p_i \to \mathcal{Y}$ and $\mathcal{L}^b_{i,u} : \mathcal{Y}^b_i \to \mathcal{Y}$ are temperature lifting operators. Here, only the system inflow port Γ_1 is handled by T_{dir}. We highlight that the constant contribution $\bar{\bar{u}}$ and the

Dirichlet lifting T_{dir} are parameter-independent. In the PR-RBC context, it is crucial to assemble $\bar{\bar{u}}$ and T_{dir} using their restrictions to instantiated components of the global system. By doing so, we only need to compute $\bar{\bar{u}}_i$ and $T_{\text{dir},1}$ for the elements of the library of archetype components.

3 The Port-Reduced Reduced-Basis Component Method

In this section, we extend the PR-RBC method to a nonlinear framework. We will also describe the treatment of the convective effects arising in the passive scalar equation. Here, we assume that we have an on-the-shelf FE solver that computes high-fidelity solution approximations $(u^h(\mu), T^h(\mu, \eta))$ such that $(u^h(\mu), T^h(\mu, \eta)) \approx (u(\mu), T(\mu, \eta))$. In the remainder of this paper, the FE solution will also be denoted $(u(\mu), T(\mu, \eta))$ to lighten the notation.

3.1 Offline/Online Strategy

As in standard Reduced Basis (RB) frameworks, the overall computational procedure for the PR-RBC is split into two stages. The first is an offline stage where the PR-RBC model learns about future systems by training general components. During the offline phase, costly computations are performed once. The second is an online stage to be performed each time one wishes to compute a new solution for a given parameter pair (μ, η) and/or each time one builds a new system. We recall that the latter case is a specific feature of the PR-RBC methodology. Standard RB methods do not allow system, topology, and geometry changes online.

3.1.1 PR-RBC for the Steady State Navier-Stokes Equation

Let us first describe our method to solve the nonlinear PDE (4) in a PR-RBC context. Consider a FE space $X \subset \mathcal{X}$ of dimension $\mathcal{N}_u$, FE port spaces $X_i^p \subset \mathcal{X}_i^p$ and FE bubble spaces $X_i^b \subset \mathcal{X}_i^b$. Additionally, consider a low-dimensional reduced space $\hat{X} \subset X$ of dimension N_u, reduced port spaces $\hat{X}_i^p \subset X_i^p$, and reduced bubble spaces $\hat{X}_i^b \subset X_i^b$. The construction of such spaces is addressed in Section 3.3 below. For offline FE solving, we also use a FE space $Q \subset \mathcal{Q}$ of dimension $\mathcal{N}_q$. In order to ensure the solvability of (4), including the divergence-free requirement (4b) and a unity-flowrate at the interfaces, we choose the velocity space to be the P2-bubble space and the pressure space to be the P1-discontinuous space. As is customary in RB contexts, the cardinality of $\hat{X}$ is such that $N_u \ll \mathcal{N}_u$. In the PR-RBC context, $\hat{X}$ also satisfies

$$\hat{X} = \bigoplus_{i=2}^{M} \mathcal{L}_{i,u}^p(\hat{X}_i^p) \oplus \bigoplus_{i=1}^{M} \mathcal{L}_{i,u}^b(\hat{X}_i^b) = \operatorname{span}\{\zeta_1, \dots, \zeta_{N_u}\}, \tag{17}$$

where $\{\zeta_1, \dots, \zeta_{N_u}\} \subset X$ is the set of port and bubble modes. For $\mu \in \mathcal{P}_{\text{Re}}$, we search for a good approximation at convergence $\hat{u}(\mu) \approx u(\mu)$ under the form

$$\hat{u}(\mu) = \bar{\bar{u}} + \sum_{i=2}^{M} \mathcal{L}_{i,u}^p \hat{u}_i^p(\mu) + \sum_{i=1}^{M} \mathcal{L}_{i,u}^b \hat{u}_i^b(\mu), \tag{18}$$

with $\hat{u}_i^p(\mu) \in \hat{X}_i^p$ and $\hat{u}_i^b(\mu) \in \hat{X}_i^b$. We introduce the PR-RBC velocity contribution

$$\tilde{u}(\mu) := \sum_{i=2}^{M} \mathcal{L}_{i,u}^p \hat{u}_i^p(\mu) + \sum_{i=1}^{M} \mathcal{L}_{i,u}^b \hat{u}_i^b(\mu) = \sum_{n=1}^{N_u} \tilde{u}_n(\mu)\zeta_n, \tag{19}$$

where $\{\tilde{u}_n(\mu)\}_{1 \leqslant n \leqslant N_u}$ are the PR-RBC velocity coefficients. Thus, the PR-RBC approximation of the velocity field (18) can be written

$$\hat{u}(\mu) = \bar{\bar{u}} + \tilde{u}(\mu). \tag{20}$$

We use a Newton algorithm to retrieve $\tilde{u}(\mu)$. At each new iteration r, the PR-RBC velocity contribution $\tilde{u}^r(\mu)$ is improved using the current increment $\hat{\delta}^r(\mu)$

$$\tilde{u}^r(\mu) = \tilde{u}^{r-1}(\mu) + \hat{\delta}^r(\mu), \tag{21}$$

where $\tilde{u}^{r-1}(\mu)$ is the PR-RBC velocity contribution at the previous iteration $r-1$. The Newton algorithm terminates once a user-specified tolerance ϵ has been reached. If based on the relative error, the stopping criterion reads $\|\tilde{u}^r(\mu) - \tilde{u}^{r-1}(\mu)\|_{\mathcal{X}} / \|\tilde{u}^r(\mu)\|_{\mathcal{X}} < \epsilon$. For $\mu \in \mathcal{P}_{\mathrm{Re}}$, each Newton iteration consists in solving the linear problem: find $\tilde{u}^r(\mu)$ such that, for all $m \in \{1, \ldots, N_u\}$,

$$a_l(\mu; \tilde{u}^r(\mu), \zeta_m) + a_{nl}(\tilde{u}^r(\mu), \tilde{u}^{r-1}(\mu), \zeta_m) + a_{nl}(\tilde{u}^{r-1}(\mu), \tilde{u}^r(\mu), \zeta_m) = a_{nl}(\tilde{u}^{r-1}(\mu), \tilde{u}^{r-1}(\mu), \zeta_m). \tag{22}$$

Using a Galerkin projection, a direct expansion of (22) leads to

$$\begin{aligned} &\sum_{n=1}^{N_u} \tilde{u}_n^r(\mu) a_l(\mu; \zeta_n, \zeta_m) + \sum_{\substack{n=1 \\ n'=1}}^{N_u} \tilde{u}_n^r(\mu) \tilde{u}_{n'}^{r-1}(\mu) a_{nl}(\zeta_n, \zeta_{n'}, \zeta_m) + \sum_{\substack{n=1 \\ n'=1}}^{N_u} \tilde{u}_n^{r-1}(\mu) \tilde{u}_{n'}^r(\mu) a_{nl}(\zeta_n, \zeta_{n'}, \zeta_m) \\ &\quad + \sum_{n=1}^{N_u} \tilde{u}_n^r(\mu) a_{nl}(\zeta_n, \bar{\bar{u}}, \zeta_m) + \sum_{n'=1}^{N_u} \tilde{u}_{n'}^r(\mu) a_{nl}(\bar{\bar{u}}, \zeta_{n'}, \zeta_m) \\ &\quad = -a_l(\mu; \bar{\bar{u}}, \zeta_m) - a_{nl}(\bar{\bar{u}}, \bar{\bar{u}}, \zeta_m) + \sum_{\substack{n=1 \\ n'=1}}^{N_u} \tilde{u}_n^{r-1}(\mu) \tilde{u}_{n'}^{r-1}(\mu) a_{nl}(\zeta_n, \zeta_{n'}, \zeta_m), \quad \forall\, 1 \leqslant m \leqslant N_u. \end{aligned} \tag{23}$$

We can now derive the algebraic formulation of (23). We introduce the parameter-independent matrices in $\mathbb{R}^{N_u\times N_u}$

$$\hat{\mathbf{K}}^u = (a_l(1;\zeta_n,\zeta_m))_{1\leqslant m,n\leqslant N_u} = \left(\int_\Omega \nabla\zeta_n\cdot\nabla\zeta_m\right)_{1\leqslant m,n\leqslant N_u}, \tag{24}$$

$$\hat{\mathbf{A}}^0_{n'} = (a_{nl}(\zeta_n,\zeta_{n'},\zeta_m))_{1\leqslant m,n\leqslant N_u} = \left(\int_\Omega (\zeta_n\cdot\nabla\zeta_{n'})\zeta_m\right)_{1\leqslant m,n\leqslant N_u}, \quad \forall n'\in\{1,\ldots,N_u\}, \tag{25}$$

$$\hat{\mathbf{B}}^0_{n} = (a_{nl}(\zeta_n,\zeta_{n'},\zeta_m))_{1\leqslant m,n'\leqslant N_u} = \left(\int_\Omega (\zeta_n\cdot\nabla\zeta_{n'})\zeta_m\right)_{1\leqslant m,n'\leqslant N_u}, \quad \forall n\in\{1,\ldots,N_u\}, \tag{26}$$

and

$$\hat{\mathbf{A}}^1 = (a_{nl}(\zeta_n,\bar{\bar{u}},\zeta_m))_{1\leqslant m,n\leqslant N_u} = \left(\int_\Omega (\zeta_n\cdot\nabla\bar{\bar{u}})\zeta_m\right)_{1\leqslant m,n\leqslant N_u}, \tag{27}$$

$$\hat{\mathbf{B}}^1 = (a_{nl}(\bar{\bar{u}},\zeta_{n'},\zeta_m))_{1\leqslant m,n'\leqslant N_u} = \left(\int_\Omega (\bar{\bar{u}}\cdot\nabla\zeta_{n'})\zeta_m\right)_{1\leqslant m,n'\leqslant N_u}. \tag{28}$$

We also introduce the parameter-independent vectors in $\mathbb{R}^{N_u}$

$$\hat{\mathbf{g}}^1 = (a_l(1;\bar{\bar{u}},\zeta_m))_{1\leqslant m\leqslant N_u} = \left(\int_\Omega \nabla\bar{\bar{u}}\cdot\nabla\zeta_m\right)_{1\leqslant m\leqslant N_u}, \tag{29}$$

$$\hat{\mathbf{g}}^2 = (a_{nl}(\bar{\bar{u}},\bar{\bar{u}},\zeta_m))_{1\leqslant m\leqslant N_u} = \left(\int_\Omega (\bar{\bar{u}}\cdot\nabla\bar{\bar{u}})\zeta_m\right)_{1\leqslant m\leqslant N_u}, \tag{30}$$

and the parameter-dependent vector in $\mathbb{R}^{N_u}$

$$\begin{aligned}\hat{\mathbf{g}}^{0,r}(\mu) &= \left(\sum_{\substack{n=1\\ n'=1}}^{N_u} \tilde{u}_n^{r-1}(\mu)\tilde{u}_{n'}^{r-1}(\mu)a_{nl}(\zeta_n,\zeta_{n'},\zeta_m)\right)_{1\leqslant m\leqslant N_u},\\ &= \left(\sum_{\substack{n=1\\ n'=1}}^{N_u} \tilde{u}_n^{r-1}(\mu)\tilde{u}_{n'}^{r-1}(\mu)\left(\int_\Omega (\zeta_n\cdot\nabla\zeta_{n'})\zeta_m\right)\right)_{1\leqslant m\leqslant N_u}.\end{aligned} \tag{31}$$

For all $m\in\{1,\ldots,N_u\}$, we introduce the matrices

$$\hat{\mathbf{C}}_m := (a_{nl}(\zeta_n,\zeta_{n'},\zeta_m))_{1\leqslant n,'n\leqslant N_u} = \left(\int_\Omega (\zeta_n\cdot\nabla\zeta_{n'})\zeta_m\right)_{1\leqslant n,'n\leqslant N_u}, \quad \in\mathbb{R}^{N_u\times N_u}. \tag{32}$$

Let $\tilde{\mathbf{u}}^r(\mu) = (\tilde{u}_n^r(\mu))_{1\leqslant n\leqslant N_u}\in\mathbb{R}^{N_u}$ be the component vector at iteration r for $\mu\in\mathcal{P}_{\mathrm{Re}}$. The vector $\hat{\mathbf{g}}^{0,r}(\mu)$ in (31) can be computed as $\hat{\mathbf{g}}^{0,r}(\mu) = \left(\tilde{\mathbf{u}}^{r-1}(\mu)^T\hat{\mathbf{C}}_m\tilde{\mathbf{u}}^{r-1}(\mu)\right)_{1\leqslant m\leqslant N_u}$. Hence, the algebraic counterpart of the right hand side in (23) is

$$\hat{\mathbf{g}}^r(\mu) = -\frac{1}{\mu}\hat{\mathbf{g}}^1 - \hat{\mathbf{g}}^2 + \hat{\mathbf{g}}^{0,r}(\mu). \tag{33}$$

Moreover, the matrix of the left hand side in (23) is

$$\hat{\mathbf{M}}^r(\mu) = \frac{1}{\mu}\hat{\mathbf{K}}^u + \sum_{n'=1}^{N_u} \tilde{u}_{n'}^{r-1}(\mu)\hat{\mathbf{A}}_{n'}^0 + \sum_{n=1}^{N_u} \tilde{u}_n^{r-1}(\mu)\hat{\mathbf{B}}_n^0 + \hat{\mathbf{A}}^1 + \hat{\mathbf{B}}^1. \tag{34}$$

Consequently, the algebraic formulation of (23) is given by

$$\hat{\mathbf{M}}^r(\mu)\tilde{\mathbf{u}}^r(\mu) = \hat{\mathbf{g}}^r(\mu). \tag{35}$$

Once the stopping criterion for the Newton algorithm has been reached, we set $\tilde{\mathbf{u}}(\mu) = \tilde{\mathbf{u}}^r(\mu)$. The final PR-RBC velocity field is assembled as

$$\hat{\mathbf{u}}(\mu) = \bar{\bar{\mathbf{u}}} + \hat{\mathbf{X}}\tilde{\mathbf{u}}(\mu), \tag{36}$$

where $\hat{\mathbf{u}}(\mu)$, $\bar{\bar{\mathbf{u}}}$ and $\tilde{\mathbf{u}}(\mu)$ are respectively the algebraic counterparts of $\hat{u}(\mu)$, $\bar{\bar{u}}$ and $\tilde{u}(\mu)$. Similarly, $\hat{\mathbf{X}}$ is the algebraic form of the PR-RBC velocity basis $\hat{X}$. The elements of $\hat{\mathbf{X}}$ are given by $\hat{\mathbf{X}}_{ij} = \hat{X}_{ij}$, where $\hat{X}_{ij}$ is the j-th coordinate of the i-th finite element basis vector. As opposed to the linear context, static condensation doesn't apply and port and bubble degrees of freedom are coupled in the same system (35). During the offline stage, we identify the quantities to be computed once and for all. We perform the following steps for every single reference port/bubble. We first compute the port and bubble sub-blocks of $\hat{\mathbf{X}}$ (cf. Sections 3.3.2 and 3.3.3 below). Then, we compute the port and bubble sub-blocks of the matrices $\hat{\mathbf{K}}^u, \hat{\mathbf{A}}^1, \hat{\mathbf{B}}^1, \{\hat{\mathbf{A}}_{n'}^0\}_{1\leqslant n'\leqslant N_u}, \{\hat{\mathbf{B}}_n^0\}_{1\leqslant n\leqslant N_u}$, and $\{\hat{\mathbf{C}}_m\}_{1\leqslant m\leqslant N_u}$. We also compute the port and bubble sub-blocks of the vectors $\hat{\mathbf{g}}^1, \hat{\mathbf{g}}^2$ and $\bar{\bar{\mathbf{u}}}$. All that remains to be performed during the online stage is the following. For every new system, we form the global parameter-independent matrices and vectors using their port and bubble sub-blocks computed offline (cf. Section 3.3.4 below). Then, for every new parameter value $\mu \in \mathcal{P}_{\mathrm{Re}}$ and at each Newton iteration, we compute the vectors $\hat{\mathbf{g}}^{0,r}(\mu)$ and $\hat{\mathbf{g}}^r(\mu)$, the matrix $\hat{\mathbf{M}}^r(\mu)$, and we solve the linear N_u-dimensional problem (35). Once the Newton algorithm converges, we evaluate the final PR-RBC velocity field using (36).

It is readily verified that a nonlinear FE solution is more costly than a linear FE solution. We highlight that this comparison still holds in the PR-RBC context. In particular, the nonlinear PR-RBC solution comes at a higher offline cost compared to a standard linear PR-RBC solution. The offline cost is mainly increased due to the computation of the matrices $\{\hat{\mathbf{A}}_{n'}^0\}_{1\leqslant n'\leqslant N_u}, \{\hat{\mathbf{B}}_n^0\}_{1\leqslant n\leqslant N_u}$ and $\{\hat{\mathbf{C}}_m\}_{1\leqslant m\leqslant N_u}$ used to accommodate the quadratic nonlinearity within the online stage. However, we recall that this cost is amortized over a large number of potential online computations for a particular model, and over all models which we can and may synthesize from the library of archetype components. Finally, the visualization of the solution field is often pursued as a post-processing step. In this case, we must appeal to the full FE degrees of freedom. However, the reconstruction is performed only once for a given system and its cost is negligible compared to a single FE solution.

3.1.2 PR-RBC for the Passive Scalar Equation

Let us describe our method to solve the nonlinear PDE (5) in a PR-RBC context. Consider a FE space $Y \subset \mathcal{Y}$ of dimension $\mathcal{N}_T$, FE port spaces $Y_i^p \subset \mathcal{Y}_i^p$ and FE bubble spaces $Y_i^b \subset \mathcal{Y}_i^b$. Additionally, consider a low-dimensional reduced space $\hat{Y} \subset Y$ of dimension N_T, reduced port spaces $\hat{Y}_i^p \subset Y_i^p$, and reduced bubble spaces $\hat{Y}_i^b \subset Y_i^b$. We address the construction of such spaces in Section 3.3 below. The cardinality of $\hat{Y}$ is such that $N_T \ll \mathcal{N}_T$. The linear space $\hat{Y}$ also satisfies

$$\hat{Y} = \bigoplus_{i=2}^{M+1} \mathcal{L}_{i,T}^p(\hat{Y}_i^p) \oplus \bigoplus_{i=1}^{M} \mathcal{L}_{i,T}^b(\hat{Y}_i^b) = \operatorname{span}\{\tau_1, \ldots, \tau_{N_T}\}, \tag{37}$$

where $\{\tau_1, \ldots, \tau_{N_T}\} \subset Y$ is the set of temperature port and bubble functions. For $(\mu, \eta) \in \mathcal{P}_{\mathrm{Re}} \times \mathcal{P}_{\mathrm{Pr}}$, we search for a good approximation at convergence $\hat{T}(\mu, \eta) \approx T(\mu, \eta)$ under the form

$$\hat{T}(\mu, \eta) = T_{\mathrm{dir}} + \sum_{i=2}^{M+1} \mathcal{L}_{i,T}^p \hat{T}_i^p(\mu, \eta) + \sum_{i=1}^{M} \mathcal{L}_{i,T}^b \hat{T}_i^b(\mu, \eta), \tag{38}$$

with $\hat{T}_i^p(\mu, \eta) \in \hat{Y}_i^p$ and $\hat{T}_i^b(\mu, \eta) \in \hat{Y}_i^b$. The PR-RBC approximation of the temperature field (38) can also be written

$$\hat{T}(\mu, \eta) = T_{\mathrm{dir}} + \sum_{n=1}^{N_T} \tilde{T}_n(\mu, \eta) \tau_n. \tag{39}$$

Using a Galerkin projection, the PR-RBC formulation of the passive scalar equation (5) reads: for all $j \in \{1, \ldots, N_T\}$,

$$\sum_{i=1}^{N_T} \tilde{T}_i(\mu, \eta) \left(c(\hat{u}(\mu))(\tau_i, \tau_j) + d(\mu, \eta; \tau_i, \tau_j) \right) = -c(\hat{u}(\mu))(T_{\mathrm{dir}}, \tau_j) - d(\mu, \eta; T_{\mathrm{dir}}, \tau_j), \tag{40}$$

where, for all $i, j \in \{1, \ldots, N_T\}$,

$$\begin{aligned} c(\hat{u}(\mu))(\tau_i, \tau_j) &= c(\bar{\bar{u}})(\tau_i, \tau_j) + \sum_{n=1}^{N_u} \tilde{u}_n(\mu)\ c(\zeta_n)(\tau_i, \tau_j), \\ d(\mu, \eta; \tau_i, \tau_j) &= \frac{1}{\mu \eta} \int_\Omega \nabla \tau_i \cdot \nabla \tau_j. \end{aligned} \tag{41}$$

Let us introduce the component vector $\tilde{\mathbf{t}}(\mu,\eta) = (\tilde{T}_n(\mu,\eta))_{1\leqslant n\leqslant N_T}$, and the matrices in $\mathbb{R}^{N_T\times N_T}$

$$\begin{aligned}
\hat{\mathbf{A}}_{\bar{\bar{u}}} &= c(\bar{\bar{u}})(\tau_i,\tau_j) = \left(\int_\Omega \nabla\tau_i\cdot\bar{\bar{u}}\;\tau_j\right)_{1\leqslant j,i\leqslant N_T},\\
\hat{\mathbf{A}}_n &= c(\zeta_n)(\tau_i,\tau_j) = \left(\int_\Omega \nabla\tau_i\cdot\zeta_n\;\tau_j\right)_{1\leqslant j,i\leqslant N_T},\quad \forall n\in\{1,\dots,N_u\},\\
\hat{\mathbf{K}}^T &= d(1,1;\tau_i,\tau_j) = \left(\int_\Omega \nabla\tau_i\cdot\nabla\tau_j\right)_{1\leqslant j,i\leqslant N_T}.
\end{aligned}\tag{42}$$

We also introduce the matrix

$$\hat{\mathbf{A}}_{\mathbf{t}_{\mathrm{dir}}} = c(\zeta_n)(T_{\mathrm{dir}},\tau_j) = \left(\int_\Omega \nabla T_{\mathrm{dir}}\cdot\zeta_n\;\tau_j\right)_{1\leqslant j\leqslant N_T,1\leqslant n\leqslant N_u}\in\mathbb{R}^{N_T\times N_u},\tag{43}$$

and the vectors in $\mathbb{R}^{N_T}$

$$\begin{aligned}
\hat{\mathbf{a}}_{\bar{\bar{u}}} &= c(\bar{\bar{u}})(T_{\mathrm{dir}},\tau_j) = \left(\int_\Omega \nabla T_{\mathrm{dir}}\cdot\bar{\bar{u}}\;\tau_j\right)_{1\leqslant j\leqslant N_T},\\
\hat{\mathbf{k}}^T &= d(1,1;T_{\mathrm{dir}},\tau_j) = \left(\int_\Omega \nabla T_{\mathrm{dir}}\cdot\nabla\tau_j\right)_{1\leqslant j\leqslant N_T}.
\end{aligned}\tag{44}$$

The algebraic form of (40) reads

$$\left(\hat{\mathbf{A}}_{\bar{\bar{u}}} + \sum_{n=1}^{N_u}\tilde{u}_n(\mu)\hat{\mathbf{A}}_n + \frac{1}{\mu\eta}\hat{\mathbf{K}}^T\right)\tilde{\mathbf{t}}(\mu,\eta) = -\left(\hat{\mathbf{a}}_{\bar{\bar{u}}} + \hat{\mathbf{A}}_{\mathbf{t}_{\mathrm{dir}}}\tilde{\mathbf{u}}(\mu) + \frac{1}{\mu\eta}\hat{\mathbf{k}}^T\right).\tag{45}$$

Finally, we assemble the final temperature field as

$$\hat{\mathbf{t}}(\mu,\eta) = \mathbf{t}_{\mathrm{dir}} + \hat{\mathbf{Y}}\tilde{\mathbf{t}}(\mu,\eta),\tag{46}$$

where $\hat{\mathbf{t}}(\mu,\eta)$, $\mathbf{t}_{\mathrm{dir}}$ and $\hat{\mathbf{Y}}$ are respectively the algebraic counterparts of $\hat{T}(\mu,\eta)$, T_{dir} and $\hat{Y}$.

During the offline stage, the first step is to compute the sub-blocks corresponding to each reference port/bubble that will eventually appear in $\hat{\mathbf{Y}}$. Then, we compute the port and bubble sub-blocks of the matrices $\hat{\mathbf{K}}^T$, $\hat{\mathbf{A}}_{\bar{\bar{u}}}$, $\{\hat{\mathbf{A}}_n\}_{1\leqslant n\leqslant N_u}$, $\hat{\mathbf{A}}_{\mathbf{t}_{\mathrm{dir}}}$ and the port and bubble sub-blocks of the vectors $\hat{\mathbf{a}}_{\bar{\bar{u}}}$, $\hat{\mathbf{k}}^T$ and $\mathbf{t}_{\mathrm{dir}}$. All that remains to be performed during the online stage is to assemble the global matrices and vectors for every new system and solve the N_T-dimensional linear problem (45). Finally, we evaluate the final PR-RBC temperature field using (46). The only cost difference with the standard linear case is the additional computation of the matrices $\{\hat{\mathbf{A}}_n\}_{1\leqslant n\leqslant N_u}$.

3.2 Caloz-Raviart *a priori* Theory

We introduce the divergence-free space

$$\mathcal{X}_{\text{div}} = \{v \in \mathcal{X} \mid \text{div}(v) = 0\}, \tag{47}$$

where $\mathcal{X} := [H^1(\Omega)]^2$ as defined in Section 2. For $\mu \in \mathcal{P}$, F is a C^1 mapping such that $F(u) = a_l(\mu; u(\mu), \cdot) + a_{nl}(u(\mu), u(\mu), \cdot)$, for all $u \in \mathcal{X}_{\text{div}}$. Here, μ is omitted as an argument of F for simplicity of the presentation. We also introduce a linear form $b : \mathcal{X}_{\text{div}} \times \mathcal{X}'_{\text{div}} \to \mathbb{R}$ such that

$$\forall v \in \mathcal{X}_{\text{div}},\ \forall w \in \mathcal{X}'_{\text{div}} : \quad b(v, w) := \langle DF(u)v, w \rangle_{\mathcal{X}'_{\text{div}}, \mathcal{X}_{\text{div}}}, \tag{48}$$

where DF refers to the Fréchet derivative of F, and $\mathcal{X}'_{\text{div}}$ is the dual space of $\mathcal{X}_{\text{div}}$. We recall from Section 3.1.1 that $\dim(\hat{X}) = N_u \in \mathbb{N}^*$, and we make the following assumptions:

- $\hat{X} \to \mathcal{X}_{\text{div}}$ when $N_u \to \infty$.
- There exists a constant $\beta_{N_u} > 0$ such that

$$\beta_{N_u} = \inf_{v \in \hat{X} \setminus \{0\}} \sup_{w \in \hat{X} \setminus \{0\}} \frac{b(v, w)}{\|v\|_{\mathcal{X}_{\text{div}}} \|w\|_{\mathcal{X}_{\text{div}}}}, \tag{49}$$

and

$$\lim_{N_u \to \infty} \inf_{u_{N_u} \in \hat{X}} \beta_{N_u}^{-2} \|u - u_{N_u}\|_{\mathcal{X}_{\text{div}}} = 0. \tag{50}$$

Note that (49) is a standard stability condition for linear problems and (50) is a standard approximation property of $\mathcal{X}_{\text{div}}$ by $\hat{X}$. We also introduce

$$\gamma := \sup_{v \in \mathcal{X}_{\text{div}} \setminus \{0\}} \frac{\|DF(u)v\|_{\mathcal{X}'_{\text{div}}}}{\|v\|_{\mathcal{X}_{\text{div}}}}. \tag{51}$$

As proven in Caloz-Raviart [30], there exists N_0 such that, for all $N_u \geqslant N_0$,

$$\|u - \hat{u}_{N_u}\|_{\mathcal{X}_{\text{div}}} \leqslant \left(1 + \frac{\gamma}{\beta_{N_u}}\right) \inf_{u_{N_u} \in \hat{X}} \|u - u_{N_u}\|_{\mathcal{X}_{\text{div}}}. \tag{52}$$

The best-fit solution in $\hat{X}$ is defined as

$$\hat{u}_{N_u}^{bf} = \underset{u_{N_u} \in \hat{X}}{\text{arginf}} \ \|u - u_{N_u}\|_{\mathcal{X}_{\text{div}}}. \tag{53}$$

Remark 1 *In order to verify (53) numerically, γ is replaced by its discrete estimate γ_{N_u}.*

3.3 Offline Approximation Spaces

In this section, we address the construction of the PR-RBC spaces introduced and used in Section 3, namely the instantiated velocity spaces $\{\hat{X}_i^p\}_{2 \leqslant i \leqslant N_u} \cup \{\hat{X}_i^b\}_{1 \leqslant i \leqslant N_u}$ and temperature spaces $\{\hat{Y}_i^p\}_{2 \leqslant i \leqslant N_T+1} \cup \{\hat{Y}_i^b\}_{1 \leqslant i \leqslant N_T}$. We present a training procedure that accommodates nonlinearities. Both the velocity and temperature basis constructions consist of two tasks: port training and bubble training. These two tasks are performed sequentially. We refer to every pair of archetype components that can share the same archetype port as 'port-compatible pairs'. The training of every port-compatible pair will be performed for both the velocity and the temperature fields jointly when searching for port modes. The same applies for every archetype component when searching for bubble modes. The idea of the port training is as follows. For every archetype port in the library $\{\hat{\Gamma}_1, \ldots, \hat{\Gamma}_{n_p}\}$, we train all port-compatible pairs associated with this port using randomized input boundary conditions at the non-shared ports. For the bubble training, the main idea is to train all the (individual) components in the library of archetype components $\{\hat{\Omega}_1, \ldots, \hat{\Omega}_{n_c}\}$ using the previously computed port modes. For every archetype port or component, the resulting PR-RBC spaces will be referred to as 'reference' spaces. For simplicity of the presentation, we drop the archetype port and component indices in absence of ambiguity. We thus present the port and bubble trainings for an archetype port $\hat{\Gamma}$ and an archetype component $\hat{\Omega}$. The corresponding reference velocity spaces will be denoted $\hat{X}^p_{\text{ref}}$ and $\hat{X}^b_{\text{ref}}$ and the corresponding reference temperature spaces will be denoted $\hat{Y}^p_{\text{ref}}$ and $\hat{Y}^b_{\text{ref}}$.

3.3.1 Zero-Flowrate Random Functions

The unity-flowrate property of the PR-RBC velocity solution (18) is ensured through the constant contribution $\bar{\bar{u}}$. Since $\bar{\bar{u}}$ is a unity-flowrate and divergence-free velocity field, we infer from (18) that $\hat{u}(\mu) - \bar{\bar{u}}$ is a divergence-free field and its flowrate through the ports of the system vanishes. Thus, port basis functions need to satisfy a zero-flowrate requirement. Furthermore, these functions need to satisfy the parabolic boundary condition (4c) that we rewrite in a simplified context and a reference coordinate system as $u(\mu)(y = -1) = u(\mu)(y = 1) = 0$ (see Figure 2). Indeed, this requirement is adjusted using rotation and translation operators whenever needed. Here, our goal is to build a set of zero-flowrate basis functions $\{h_1, \ldots, h_R\}$, with $R \in \mathbb{N}^*$. These functions will be used in the port training algorithm. Let $\{L_0, L_1, \ldots\}$ be the Legendre polynomials [31], where the subscript is the degree of the polynomial. The Legendre polynomials satisfy the orthogonality property

$$\int_{-1}^{1} L_k(y) L_{k'}(y) dy = 0, \quad \forall k \neq k' \text{with } k, k' \in \mathbb{N}. \tag{54}$$

Moreover, there exist $\gamma_0, \gamma_1, \gamma_2 \in \mathbb{R}$ such that

$$1 - y^2 = \gamma_0 L_0(y) + \gamma_1 L_1(y) + \gamma_2 L_2(y). \tag{55}$$

The orthogonality property (54) then yields

$$\int_{-1}^{1} (1-y^2)L_{k'}(y)dy = 0, \qquad \forall\ k \geqslant 3. \tag{56}$$

Furthermore, it holds that

$$\int_{-1}^{1} (1-y^2)ydy = 0, \qquad \text{and} \int_{-1}^{1} (1-y^2)(5y^2-1)dy = 0. \tag{57}$$

Thus, we choose the set of weighted polynomials

$$P_k(y) = \begin{cases} (1-y^2)y, & \text{if } k = 1, \\ \dfrac{1}{4}(1-y^2)(5y^2-1), & \text{if } k = 2, \\ \dfrac{1}{k^2}(1-y^2)L_k(y), & \text{if } 3 \leqslant k \leqslant R, \end{cases} \tag{58}$$

as zero-flowrate functions for the port training algorithm.

Proposition 1 *We denote by $\mathbb{P}_R([-1,1])$ the space of polynomials of degree R with real-valued coefficients. We introduce $\mathcal{A} = \left\{Q_1 \in \mathbb{P}_{R+2}([-1,1]) \mid Q_1(1) = Q_1(-1) = 0,\ \int_{-1}^{1} Q_1 = 0\right\}$. The following properties hold true*
(i) $(\ Q_1 \in \mathcal{A}$ *and* $Q_1 \neq 0_{\mathbb{P}_{R+2}([-1,1])}\ ) \Rightarrow deg(Q_1) \geqslant 3$*;*
(ii) $\mathcal{A} = \mathrm{span}(P_1, \ldots, P_R)$*.*

Proof (i) For $Q_1 \in \mathcal{A}$ such that $Q_1 \neq 0$, we have $Q_1(1) = Q_1(-1) = 0$. Hence, $(1-y^2)$ divides Q_1. Furthermore, $\int_{-1}^{1}(1-y^2) \neq 0$. Consequently, $deg(Q_1) \geqslant 3$;
(ii) $(P_1, \ldots, P_R) \subset \mathcal{A}$ by construction. For $Q_1 \in \mathcal{A}$, $3 \leqslant deg(Q_1) \leqslant R+2$. Hence, $dim(\mathcal{A}) \leqslant R$. Furthermore, the elements in $(P_1, \ldots, P_R)$ all have different polynomial degrees. Thus, $(P_1, \ldots, P_R)$ is a linearly independent family of maximal dimension, whereof the result.

□

The chosen set satisfies the boundary conditions, but the zero-flowrate requirement is verified only at the continuous level. To ensure the requirement remains valid in a discrete setting with a FE space $X \subset [H^1(\Omega)]^2$ and an exact quadrature on the interface ports, we search for discrete functions $\{h_1, \ldots, h_R\}$ such that, for each $k \in \{1, \ldots, R\}$, h_k satisfies

$$\begin{cases} h_k = \underset{g \in X}{\mathrm{argmin}} \|g - P_k\|_X, \\ \displaystyle\int_{-1}^{1} h_k = 0. \end{cases} \tag{59}$$

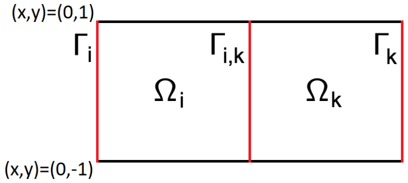

Figure 2: A pair of components used for the port training. The boundaries in black represent $\partial\Omega^{\text{wall}}$.

3.3.2 Port Training

The first step of the offline stage is the port training. A crucial requirement is the zero-flowrate condition at the ports for the velocity field. For the temperature field, we introduce a specific treatment to allow for an efficient representation of the convective effects. In order to accurately represent the solution field at the ports, we train every port-compatible pair and evaluate how the so-called 'receiving port' responds to forcing at the so-called 'sending ports'. In the linear context, optimal port spaces can be retrieved by calculating the transfer operator [13]. We cannot invoke the transfer eigenproblem in nonlinear contexts. Thus, we pursue a probabilistic approach based on random forcing [32]. The approach was originally applied to a linear problem in [10], and more recently rigorously related to the transfer eigenproblem for linear problems [33].

For $i, k \in \{1, \dots, n_c\}$, we denote by $\Omega_{i,k} = \Omega_i \cup \Omega_k$ the physical domain of a port-compatible pair of interest, by Γ_i the sending port on Ω_i, by Γ_k the sending port on Ω_k, and by $\Gamma_{i,k}$ the receiving port. Figure 2 illustrates a pair of components to be trained in a simplified setting. We also denote by $\mathcal{O}^{\mathcal{D}}_{\Gamma_i,\Gamma_k}(\mu;\omega_i,\omega_k)$ the discrete solution to the steady state Navier–Stokes problem for a parameter $\mu \in \mathcal{P}_{\text{Re}}$, in a domain $\mathcal{D}$, for the boundary conditions ω_i on Γ_i and ω_k on Γ_k, and for homogeneous Dirichlet boundary conditions on $\partial\Omega^{\text{wall}}$ and $\partial\Omega^{\text{cavity}}$. Let $\mathcal{P}^{\text{tr}}_{\text{Re}} = \{\mu_1, \dots, \mu_{n_u^{\text{tr}}}\} \subset \mathcal{P}_{\text{Re}}$ be a discrete training set and let $n_f \in \mathbb{N}^*$. The idea is to use a set of input forcing functions $\{\omega_i^1, \dots, \omega_i^{n_f}\}$ and $\{\omega_k^1, \dots, \omega_k^{n_f}\}$ as Dirichlet boundary conditions at the sending ports and collect the set of solutions at the receiving port

$$\tilde{\mathcal{M}}_u = \left\{\mathcal{O}^{\Omega_{i,k}}_{\Gamma_i,\Gamma_k}(\mu;\omega_i^l,\omega_k^l)|_{\Gamma_{i,k}} \mid \mu \in \mathcal{P}^{\text{tr}}_{\text{Re}}, 1 \leqslant l \leqslant n_f\right\}. \tag{60}$$

In order to account for the constant flowrate of the velocity field in the flow direction (i.e., normal direction with regard to the interface ports), the input forcing functions are chosen under the form

$$\omega_i^l = \begin{pmatrix} \bar{u}_i + \sum_{r=1}^R \kappa_{i,r}^l h_r \\ z_i^l \end{pmatrix}, \quad \text{and } \omega_k^l = \begin{pmatrix} \bar{u}_k + \sum_{r=1}^R \kappa_{k,r}^l h_r \\ z_k^l \end{pmatrix}, \qquad \forall\, 1 \leqslant l \leqslant n_f. \tag{61}$$

The random coefficients $\kappa_{i,r}^l$ and $\kappa_{k,r}^l$ are generated using a normal distribution of mean 0 and variance 1 and the functions $\{h_r\}_{1\leqslant r\leqslant R}$ are the set of zero-flowrate polynomials introduced in 3.3.1. Here, z_i^l and z_k^l are random functions in the tangential direction which can be generated using a user-defined basis of functions. In our numerical test cases, z_i^l and z_k^l are linear combinations of $\{h_r\}_{1\leqslant r\leqslant R}$ with coefficients generated using a normal distribution of mean 0 and variance 1. Indeed, (61) is expressed in an orthonormal coordinate system where the first axis is in the flow direction. The input functions ω_i^l and ω_k^l are rotated and translated using appropriate operators whenever needed. The flowrate conservation imposed at the sending ports (61) ensures the existence of $\mathcal{O}^{\Omega_{i,k}}_{\Gamma_i,\Gamma_k}(\mu;\omega_i^l,\omega_k^l)$in (60) . For a given port Γ, we introduce a zero-flowrate $H^{\frac{1}{2}}$-projection operator on Γ denoted Π^0_Γ. We can then compute the set

$$\mathcal{M}_u = \left\{ \Pi^0_{\Gamma_{i,k}}\left(v-\bar{u}_{i,k}\right) \mid v\in\tilde{\mathcal{M}}_u \right\}, \tag{62}$$

which collects the projections of the solutions on the interface port $\Gamma_{i,k}$ after subtracting the unity-flowrate contribution $\bar{u}_{i,k}$, thereby yielding zero-flowrate port functions. The velocity port modes are obtained via a compression of $\mathcal{M}_u$ by means of the Proper Orthogonal Decomposition (POD) [34, 35]

$$\{\chi_1,\ldots,\chi_{N_u^p}\} = \texttt{POD}\left(\mathcal{M}_u,\varepsilon_u^p\right), \tag{63}$$

where ε_u^p is the relative truncation threshold of the POD. Finally, the reference velocity port space is defined as

$$\hat{X}^p_{\text{ref}} = \text{span}\{\chi_1,\ldots,\chi_{N_u^p}\}. \tag{64}$$

Note that the zero-flowrate condition is satisfied for the port modes resulting from the POD in (63). In fact, $\hat{X}^p_{\text{ref}} \subset \text{span}\{\mathcal{M}_u\}$, and the elements in $\mathcal{M}_u$ satisfy the zero-flowrate criterion by construction.

Let us now describe the construction of the temperature PR-RBC port spaces. We denote by $\mathcal{H}^{\mathcal{D}}_{\Gamma_i,\Gamma_k}(\mu,\eta;\omega_i,\omega_k,\lambda_i)$ the discrete solution of the passive scalar equation in a domain $\mathcal{D}$. Given the velocity field $\mathcal{O}^{\mathcal{D}}_{\Gamma_i,\Gamma_k}(\mu;\omega_i,\omega_k)$, the discrete temperature field $\mathcal{H}^{\mathcal{D}}_{\Gamma_i,\Gamma_k}(\mu,\eta;\omega_i,\omega_k,\lambda_i)$ is computed for a parameter $\eta\in\mathcal{P}_{\text{Pr}}$, the Dirichlet boundary condition λ_i on Γ_i, a homogeneous Neumann boundary condition on Γ_k and $\partial\Omega^{\text{wall}}$, and a homogeneous Dirichlet boundary condition on $\partial\Omega^{\text{cavity}}$. Let $\mathcal{P}^{\text{tr}}_{\text{Pr}} = \{\eta_1,\ldots,\eta_{n_T^{\text{tr}}}\}\subset\mathcal{P}_{\text{Pr}}$ be a discrete training set. The idea is to use a set of input functions $\{\lambda_i^1,\ldots,\lambda_i^{n_{\text{test}}}\}$ as inflow Dirichlet boundary conditions and collect the set of solutions at the receiving port

$$\mathcal{M}_T = \left\{ \mathcal{H}^{\Omega_{i,k}}_{\Gamma_i,\Gamma_k}(\mu,\eta;\omega_i^l,\omega_k^l,\lambda_i^l)|_{\Gamma_{i,k}} \mid \mu\in\mathcal{P}^{\text{tr}}_{\text{Re}}, \eta\in\mathcal{P}^{\text{tr}}_{\text{Pr}}, 1\leqslant l\leqslant n_f \right\}. \tag{65}$$

We highlight that, unlike for the velocity training, the temperature training is performed with natural boundary conditions at outflow for a good representation of the convective effects, and also to avoid resolution requirements of artificial boundary layers (see Figure 3). The reference

Figure 3: Forcing boundary conditions with forcing ports in red and receiving ports in blue. Left: For the velocity. Right: For the temperature.

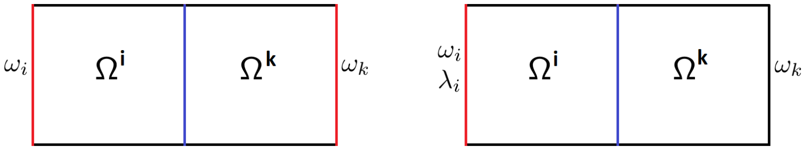

temperature port modes result from a compression of $\mathcal{M}_T$ by means of the POD

$$\{\phi_1, \ldots, \phi_{N_T^p}\} = \mathtt{POD}\,(\mathcal{M}_T, \varepsilon_T^p)\,, \tag{66}$$

where ε_T^p is the relative truncation threshold of the POD. Finally, the reference temperature port space is defined as

$$\hat{Y}_{\text{ref}}^p = \text{span}\{\phi_1, \ldots, \phi_{N_T^p}\}. \tag{67}$$

The port training is detailed in Algorithm 1. We recall that Algorithm 1 has to be run for every single archetype port in the library $\{\hat{\Gamma}_1, \ldots, \hat{\Gamma}_{n^p}\}$, i.e., for every port-compatible pair of components for this port.

Algorithm 1 `PORT_TRAINING`

```
Input: $\mathcal{P}_{\mathrm{Re}}^{\mathrm{tr}} \times \mathcal{P}_{\mathrm{Pr}}^{\mathrm{tr}}$: training set
       $\Omega_{i,k}$: pair of components
       $\Gamma_{i,k}$: receiving port
       $\varepsilon_u^p, \varepsilon_T^p$: POD truncation thresholds
       $n_f$: number of forcing functions
for $1 \leqslant l \leqslant n_f$ do
    for $\mu \in \mathcal{P}_{\mathrm{Re}}^{\mathrm{tr}}$ do
        Compute $\mathcal{O}_{\Gamma_i,\Gamma_k}^{\Omega_{i,k}}(\mu; \omega_i^l, \omega_k^l)|_{\Gamma_{i,k}}$
        for $\eta \in \mathcal{P}_{\mathrm{Pr}}^{\mathrm{tr}}$ do
            Compute $\mathcal{H}_{\Gamma_i,\Gamma_k}^{\Omega_{i,k}}(\mu, \eta; \omega_i^l, \omega_k^l, \lambda_i^l)$
        end for
    end for
end for
Set $\tilde{\mathcal{M}}_u = \left\{ \mathcal{O}_{\Gamma_i,\Gamma_k}^{\Omega_{i,k}}(\mu; \omega_i^l, \omega_k^l)|_{\Gamma_{i,k}} \mid \mu \in \mathcal{P}_{\mathrm{Re}}^{\mathrm{tr}}, 1 \leqslant l \leqslant n_f \right\}$
Set $\mathcal{M}_u = \left\{ \Pi_{\Gamma_{i,k}}^0 \left(v - \bar{u}_{i,k}\right) \mid v \in \tilde{\mathcal{M}}_u \right\}$
Compute $\{\chi_1, \ldots, \chi_{N_u^p}\} = \mathtt{POD}\left(\mathcal{M}_u, \varepsilon_u^p\right)$
Set $\hat{X}_{\mathrm{ref}}^p = \mathrm{span}\{\chi_1, \ldots, \chi_{N_u^p}\}$
Set $\mathcal{M}_T = \left\{ \mathcal{H}_{\Gamma_i,\Gamma_k}^{\Omega_{i,k}}(\mu, \eta; \omega_i^l, \omega_k^l, \lambda_i^l)|_{\Gamma_{i,k}} \mid \mu \in \mathcal{P}_{\mathrm{Re}}^{\mathrm{tr}}, \eta \in \mathcal{P}_{\mathrm{Pr}}^{\mathrm{tr}}, 1 \leqslant l \leqslant n_f \right\}$
Compute $\{\phi_1, \ldots, \phi_{N_T^p}\} = \mathtt{POD}\left(\mathcal{M}_T, \varepsilon_T^p\right)$
Set $\hat{Y}_{\mathrm{ref}}^p = \mathrm{span}\{\phi_1, \ldots, \phi_{N_T^p}\}$

Output: $\hat{X}_{\mathrm{ref}}^p = \{\chi_1, \ldots, \chi_{N_u^p}\}$: velocity port space
        $\hat{Y}_{\mathrm{ref}}^p = \{\phi_1, \ldots, \phi_{N_T^p}\}$: temperature port space
        $N_u^p$: number of velocity port modes
        $N_T^p$: number of temperature port modes
```

To increase computational efficiency, we suggest an improvement of the procedure described above by using a simplified version of the hierarchical POD [36]. In practice, for each parameter value $\mu \in \mathcal{P}_{\mathrm{Re}}^{\mathrm{tr}}$, we first form the parameter-dependent set

$$\tilde{\mathcal{M}}_u(\mu) = \left\{ \mathcal{O}_{\Gamma_i,\Gamma_k}^{\Omega_{i,k}}(\mu; \omega_i^l, \omega_k^l)|_{\Gamma_{i,k}} \mid 1 \leqslant l \leqslant n_f \right\}. \tag{68}$$

Then, we compute its zero-flowrate counterpart

$$\mathcal{M}_u(\mu) = \left\{ \Pi_{\Gamma_{i,k}}^0 \left(v - \bar{u}_{i,k}\right) \mid v \in \tilde{\mathcal{M}}_u(\mu) \right\}. \tag{69}$$

At this stage, we compute the parameter-dependent vectors

$$\{\tilde{\chi}_1(\mu), \ldots, \tilde{\chi}_{\tilde{N}_u^p(\mu)}(\mu)\} := \mathtt{POD}(\mathcal{M}_u(\mu), \varepsilon_u^p), \tag{70}$$

and the corresponding singular values

$$\{s_1(\mu), \ldots, s_{\tilde{N}_u^p(\mu)}(\mu)\} = \mathtt{singular\_values}(\{\tilde{\chi}_1(\mu), \ldots, \tilde{\chi}_{\tilde{N}_u^p(\mu)}(\mu)\}, \varepsilon_u^p). \tag{71}$$

We use the singular values $\{s_1(\mu), \ldots, s_{\tilde{N}_u^p(\mu)}(\mu)\}$ to scale the modes $\{\tilde{\chi}_1(\mu), \ldots, \tilde{\chi}_{N_u^p(\mu)}(\mu)\}$ before performing a final POD

$$\{\chi_1, \ldots, \chi_{N_u^p}\} = \texttt{POD}\left(\bigcup_{\mu \in \mathcal{P}_{\mathrm{Re}}^{\mathrm{tr}}} \{s_1(\mu)\tilde{\chi}_1(\mu), \ldots, s_{\tilde{N}_u^p(\mu)}(\mu)\tilde{\chi}_{\tilde{N}_u^p(\mu)}(\mu)\}, \varepsilon_u^p\right). \tag{72}$$

Consequently, the reference velocity port space using a hierarchical POD is given by

$$\hat{X}_{\mathrm{ref}}^p = \mathrm{span}\{\chi_1, \ldots, \chi_{N_u^p}\}. \tag{73}$$

In terms of computational effort, the POD in (66) requires the solution of an eigenproblem of dimension $n_f \times \mathrm{Card}(\mathcal{P}_{\mathrm{Re}}^{\mathrm{tr}})$, whereas (72) requires the solution of n_f eigenproblems of dimension $\mathrm{Card}(\mathcal{P}_{\mathrm{Re}}^{\mathrm{tr}})$. It is readily verified that the latter strategy is computationally more efficient than the former. The computational efficiency of the temperature port training is improved in the same fashion. The port training using the hierarchical POD for both the velocity and the temperature is described in Algorithm 2.

Remark 2 *For the temperature port training, we perform some additional steps for components likely to appear at system inflow or system outflow ends of the potential online geometries. We recall that 'system' refers to the geometry that will be built online. For single components (not a pair of components), we train with the inflow port being the sending port and the outflow port being the receiving port. Training single components is mainly considered to accommodate the specific case of a single-component online geometry. For pairs of components, we train with the target Dirichlet boundary condition at inflow and a Neumann boundary condition at outflow. We amend the port space with the resulting port modes. In riverine contexts, these steps are performed for channel components (either as a single component or as a component appearing at inflow or outflow of a pair of components) and is usually skipped for bends.*

3.3.3 Bubble Training

We also use the idea of random forcing to train the bubbles. Unlike for port training, the bubble training is performed for a single component at a time. We present a basis construction that satisfies the incompressibility condition for the velocity bubbles, thereby ensuring the incompressibility condition for the final velocity field to be computed during the online stage. We define $\psi_{\Gamma_i \to \hat{\Omega}_i} : X_i^p \to X_i^b$ as the left port Stokes lifting operator into $\hat{\Omega}_i$, i.e., $\psi_{\Gamma_i \to \hat{\Omega}_i}(\xi_u)$ is the solution to

$$a_l(1; \psi_{\Gamma_i \to \hat{\Omega}_i}(\xi_u), v) - b(p, v) = 0, \qquad \forall v \in X_i^b, \tag{74a}$$

$$b(q, \psi_{\Gamma_i \to \hat{\Omega}_i}(\xi_u)) = 0, \qquad \forall q \in Q_i, \tag{74b}$$

$$\psi_{\Gamma_i \to \hat{\Omega}_i}(\xi_u) = \xi_u, \qquad \text{on } \Gamma_i, \tag{74c}$$

$$\psi_{\Gamma_i \to \hat{\Omega}_i}(\xi_u) = 0, \qquad \text{on } \partial\hat{\Omega}^{\mathrm{wall}} \cup \partial\hat{\Omega}^{\mathrm{cavity}} \cup \Gamma_{i+1}, \tag{74d}$$

Algorithm 2 `DISTRIBUTED_PORT_TRAINING`

```
Input: $\mathcal{P}^{\rm tr}_{\rm Re} \times \mathcal{P}^{\rm tr}_{\rm Pr}$: training set
       $\Omega_{i,k}$: pair of components
       $\Gamma_{i,k}$: receiving port
       $\varepsilon^p_u, \varepsilon^p_T$: POD truncation thresholds
       $n_f$: number of forcing functions
for $\mu \in \mathcal{P}^{\rm tr}_{\rm Re}$ do
    for $1 \leqslant l \leqslant n_f$ do
        Compute $\mathcal{O}^{\Omega_{i,k}}_{\Gamma_i,\Gamma_k}(\mu; \omega^l_i, \omega^l_k)|_{\Gamma_{i,k}}$
        for $\eta \in \mathcal{P}^{\rm tr}_{\rm Pr}$ do
            Compute $\mathcal{H}^{\Omega_{i,k}}_{\Gamma_i,\Gamma_k}(\mu, \eta; \omega^l_i, \omega^l_k, \lambda^l_i)$
        end for
    end for
    Set $\tilde{\mathcal{M}}_u(\mu) = \left\{\mathcal{O}^{\Omega_{i,k}}_{\Gamma_i,\Gamma_k}(\mu; \omega^l_i, \omega^l_k)|_{\Gamma_{i,k}} \mid 1 \leqslant l \leqslant n_f\right\}$
    Compute $\mathcal{M}_u(\mu) = \left\{\Pi^0_{\Gamma_{i,k}}\left(v - \bar{u}_{i,k}\right) \mid v \in \tilde{\mathcal{M}}_u(\mu)\right\}$
    Compute $\{\tilde{\chi}_1(\mu), \ldots, \tilde{\chi}_{\tilde{N}^p_u(\mu)}(\mu)\} := \texttt{POD}(\mathcal{M}_u(\mu), \varepsilon^p_u)$
    Set $\{s_1(\mu), \ldots, s_{\tilde{N}^p_u(\mu)}(\mu)\} = \texttt{singular\_values}(\{\tilde{\chi}_1(\mu), \ldots, \tilde{\chi}_{\tilde{N}^p_u(\mu)}(\mu)\}, \varepsilon^p_u)$
    Set $\mathcal{M}_T(\eta) = \left\{\mathcal{H}^{\Omega_{i,k}}_{\Gamma_i,\Gamma_k}(\mu, \eta; \omega^l_i, \omega^l_k, \lambda^l_i) \mid 1 \leqslant l \leqslant n_f,\ \eta \in \mathcal{P}^{\rm tr}_{\rm Pr}\right\}$
    Compute $\{\tilde{\phi}_1(\eta), \ldots, \tilde{\phi}_{\tilde{N}^p_T(\eta)}(\eta)\} := \texttt{POD}(\mathcal{M}_T(\eta), \varepsilon^p_T)$
    Set $\{\sigma_1(\eta), \ldots, \sigma_{\tilde{N}^p_T(\eta)}(\eta)\} = \texttt{singular\_values}(\{\tilde{\phi}_1(\eta), \ldots, \tilde{\phi}_{\tilde{N}^p_T(\eta)}(\eta)\}, \varepsilon^p_T)$
end for
Compute $\{\chi_1, \ldots, \chi_{N^p_u}\} = \texttt{POD}\left(\bigcup_{\mu \in \mathcal{P}^{\rm tr}_{\rm Re}} \{s_1(\mu)\tilde{\chi}_1(\mu), \ldots, s_{\tilde{N}^p_u(\mu)}(\mu)\tilde{\chi}_{\tilde{N}^p_u(\mu)}(\mu)\}, \varepsilon^p_u\right)$
Set $\hat{X}^p_{\rm ref} = {\rm span}\{\chi_1, \ldots, \chi_{N^p_u}\}$
Compute $\{\phi_1, \ldots, \phi_{N^p_T}\} = \texttt{POD}\left(\bigcup_{\eta \in \mathcal{P}^{\rm tr}_{\rm Pr}} \{\sigma_1(\eta)\tilde{\phi}_1(\eta), \ldots, \sigma_{\tilde{N}^p_T(\eta)}(\eta)\tilde{\phi}_{\tilde{N}^p_T(\mu)}(\eta)\}, \varepsilon^p_T\right)$
Set $\hat{Y}^p_{\rm ref} = {\rm span}\{\phi_1, \ldots, \phi_{N^p_T}\}$
Output: $\hat{X}^p_{\rm ref} = \{\chi_1, \ldots, \chi_{N^p_u}\}$: velocity port space
        $\hat{Y}^p_{\rm ref} = \{\phi_1, \ldots, \phi_{N^p_T}\}$: temperature port space
        $N^p_u$: dimension of the velocity port space
        $N^p_T$: dimension of the temperature port space
```

where $Q_i \subset \mathcal{Q}_i$ is a FE discretization space. Similarly, $\psi_{\Gamma_{i+1} \to \hat{\Omega}_i} : X^p_{i+1} \to X^b_i$ is the right port Stokes lifting operator into $\hat{\Omega}_i$, i.e., $\psi_{\Gamma_{i+1} \to \hat{\Omega}_i}(\xi_u)$ is the solution to

$$a_l(1; \psi_{\Gamma_{i+1} \to \hat{\Omega}_i}(\xi_u), v) - b(p, v) = 0, \qquad \forall v \in X^b_i, \tag{75a}$$

$$b(q, \psi_{\Gamma_{i+1} \to \hat{\Omega}_i})(\xi_u) = 0, \qquad \forall q \in Q_i, \tag{75b}$$

$$\psi_{\Gamma_{i+1} \to \hat{\Omega}_i}(\xi_u) = \xi_u, \qquad \text{on } \Gamma_{i+1}, \tag{75c}$$

$$\psi_{\Gamma_{i+1} \to \hat{\Omega}_i}(\xi_u) = 0, \qquad \text{on } \partial\hat{\Omega}^{\rm wall} \cup \partial\hat{\Omega}^{\rm cavity} \cup \Gamma_i. \tag{75d}$$

Since the port training has already been performed, an efficient and goal-oriented bubble training should not use fully random functions at the ports of a component for forcing, but rather linear combinations of the previously computed port modes. In fact, only port mode-like profiles are likely to arise at the ports. Hence, we define random input boundary conditions at the ports of component i as follows

$$\omega_i^l = \bar{u}_i + \sum_{n=1}^{N_u^p} \kappa_{i,n}^l \chi_n, \quad \text{and } \omega_{i+1}^l = \bar{u}_{i+1} + \sum_{n=1}^{N_u^p} \kappa_{i+1,n}^l \chi_n, \qquad \forall\ 1 \leqslant l \leqslant n_f, \tag{76}$$

where $\kappa_{i,n}^l$ and $\kappa_{i+1,n}^l$ are random coefficients generated using a normal distribution of mean 0 and variance 1. Then, we compute the corresponding solutions to the steady state Navier–Stokes problem

$$\tilde{\mathcal{R}}_u = \left\{ \mathcal{O}_{\Gamma_i,\Gamma_{i+1}}^{\hat{\Omega}_i}(\mu; \omega_i^l, \omega_{i+1}^l) \mid \mu \in \mathcal{P}_{\mathrm{Re}}^{\mathrm{tr}} \right\}. \tag{77}$$

In order to account for the incompressibility condition (4b), and to form the set of divergence-free bubble functions, we create

$$\mathcal{R}_u = \left\{ \mathcal{O}_{\Gamma_i,\Gamma_{i+1}}^{\hat{\Omega}_i}(\mu; \omega_i^l, \omega_{i+1}^l) - \bar{\bar{u}}_i - \sum_{n=1}^{N_u^p} \kappa_{i,n}^l \psi_{\Gamma_i \to \hat{\Omega}_i}(\chi_n) - \sum_{n=1}^{N_u^p} \kappa_{i+1,n}^l \psi_{\Gamma_{i+1} \to \hat{\Omega}_i}(\chi_n) \mid \mu \in \mathcal{P}_{\mathrm{Re}}^{\mathrm{tr}}, 1 \leqslant l \leqslant n_f \right\}.$$

Applying the POD to the set $\mathcal{R}_u$ with a truncation threshold ε_u^b , we obtain the divergence-free bubble modes

$$(\alpha_1, \ldots, \alpha_{N_u^b}) = \mathtt{POD}(\mathcal{R}_u, \varepsilon_u^b). \tag{78}$$

Finally, the reference PR-RBC velocity bubble space is given by

$$\hat{X}_{\mathrm{ref}}^b = \mathrm{span}(\alpha_1, \ldots, \alpha_{N_u^b}). \tag{79}$$

It is readily verified that the resulting bubble modes are incompressible.

Let us now describe the construction of the temperature PR-RBC bubble spaces. We define $\varphi_{\Gamma_i \to \hat{\Omega}_i} : Y_i^p \to Y_i^b$ as the left port lifting operator into $\hat{\Omega}_i$, i.e., $\varphi_{\Gamma_i \to \hat{\Omega}_i}(\xi_T)$ is the solution to

$$\int_{\hat{\Omega}} \nabla \varphi_{\Gamma_i \to \hat{\Omega}_i}(\xi_T) \cdot \nabla \theta = 0, \qquad \forall \theta \in Y_i^b, \tag{80a}$$

$$\varphi_{\Gamma_i \to \hat{\Omega}_i}(\xi_T) = \xi_T, \qquad \text{on } \Gamma_i, \tag{80b}$$

$$\varphi_{\Gamma_i \to \hat{\Omega}_i}(\xi_T) = 0, \qquad \text{on } \partial\hat{\Omega}^{\mathrm{cavity}} \cup \Gamma_{i+1}, \tag{80c}$$

$$\frac{\partial \varphi_{\Gamma_i \to \hat{\Omega}_i}(\xi_T)}{\partial n} = 0, \qquad \text{on } \partial\hat{\Omega}^{\mathrm{wall}}. \tag{80d}$$

In the same fashion, we define $\varphi_{\Gamma_{i+1}\to\hat{\Omega}_i} : Y^p_{i+1} \to Y^b_i$ as the right port lifting operator into $\hat{\Omega}_i$, i.e., $\varphi_{\Gamma_{i+1}\to\hat{\Omega}_i}(\xi_T)$ is the solution to

$$\int_{\hat{\Omega}} \nabla\varphi_{\Gamma_i\to\hat{\Omega}_i}(\xi_T)\cdot\nabla\theta = 0, \qquad \forall\theta\in Y^b_i, \tag{81a}$$

$$\varphi_{\Gamma_i\to\hat{\Omega}_i}(\xi_T) = \xi_T, \qquad \text{on } \Gamma_{i+1}, \tag{81b}$$

$$\varphi_{\Gamma_i\to\hat{\Omega}_i}(\xi_T) = 0, \qquad \text{on } \partial\hat{\Omega}^{\text{cavity}} \cup \Gamma_i, \tag{81c}$$

$$\frac{\partial\varphi_{\Gamma_i\to\hat{\Omega}_i}(\xi_T)}{\partial n} = 0, \qquad \text{on } \partial\hat{\Omega}^{\text{wall}}. \tag{81d}$$

We highlight that the boundary conditions (80c) and (81c) are chosen to better capture the convective effects. We also define random input boundary conditions at the left port of component i as follows

$$\lambda^l_i = \sum_{n=1}^{N^p_T} \kappa^l_{i,n}\phi_n, \qquad \forall\ 1\leqslant l\leqslant n_f, \tag{82}$$

where $\kappa^l_{i,n}$ are random coefficients generated using a normal distribution of mean 0 and variance 1. We compute the corresponding solutions to the passive scalar equation

$$\tilde{\mathcal{R}}_T = \left\{\mathcal{H}^{\hat{\Omega}_i}_{\Gamma_i,\Gamma_{i+1}}(\mu,\eta;\omega^l_i,\omega^l_{i+1},\lambda^l_i) \mid \mu\in\mathcal{P}^{\text{tr}}_{\text{Re}}, \eta\in\mathcal{P}^{\text{tr}}_{\text{Pr}}, 1\leqslant l\leqslant n_f\right\}. \tag{83}$$

At this stage, we subtract the left port contribution and the lifting of the solution at the right port so as to retain functions that represent the behavior of the temperature field only in the interior of the component

$$\mathcal{R}_T = \left\{\theta - \varphi_{\Gamma_i\to\hat{\Omega}_i}(\theta|_{\Gamma_i}) - \varphi_{\Gamma_{i+1}\to\hat{\Omega}_i}(\theta|_{\Gamma_{i+1}}) \mid \theta\in\tilde{\mathcal{R}}_T\right\}. \tag{84}$$

Note that for $\theta = \mathcal{H}^{\hat{\Omega}_i}_{\Gamma_i,\Gamma_{i+1}}(\mu,\eta;\omega^l_i,\omega^l_{i+1},\lambda^l_i)$, the left lifting is given by $\varphi_{\Gamma_i\to\hat{\Omega}_i}(\theta|_{\Gamma_i}) = \sum_{n=1}^{N^p_T}\kappa^l_{i,n}\varphi_{\Gamma_i\to\hat{\Omega}_i}(\phi_n)$, where the liftings $\{\varphi_{\Gamma_i\to\hat{\Omega}_i}(\phi_n)\}_{1\leqslant n\leqslant N^p_T}$ are computed only once. The temperature bubble modes result from the compression of the set $\mathcal{R}_T$ by means of a POD with a truncation threshold ε^b_T

$$\{\beta_1,\ldots,\beta_{N^b_T}\} = \texttt{POD}\left(\mathcal{R}_T,\varepsilon^b_T\right). \tag{85}$$

Finally, the reference temperature PR-RBC bubble space is defined as

$$\hat{Y}^b_{\text{ref}} = \text{span}\{\beta_1,\ldots,\beta_{N^b_T}\}. \tag{86}$$

As the procedure highlights it, the port training has to be performed prior to the bubble training. Furthermore, the bubbles are trained with natural boundary conditions at the right (outflow) port for a good representation of the convective effects. The bubble training strategy is detailed in Algorithm 3. We recall that Algorithm 3 has to be run for every archetype component in the library $\{\hat{\Omega}_1, \dots, \hat{\Omega}_{n_c}\}$.

Algorithm 3 `BUBBLE_TRAINING`

```
Input: $\mathcal{P}^{\rm tr}_{\rm Re} \times \mathcal{P}^{\rm tr}_{\rm Pr}$: training set
       $\hat{\Omega}_i$: trained component
       $\varepsilon^b_u, \varepsilon^b_T$: truncation thresholds
       $\{\chi_1, \dots, \chi_{N^p}\}$: port modes
       $n_f$: number of forcing functions
Compute $\bar{\bar{u}}_i$
Compute the velocity left port liftings $\{\psi_{\Gamma_i \to \hat{\Omega}_i}(\chi_n)\}_{1 \leqslant n \leqslant N^p_u}$
Compute the velocity right port liftings $\{\psi_{\Gamma_{i+1} \to \hat{\Omega}_i}(\chi_n)\}_{1 \leqslant n \leqslant N^p_u}$
Compute the temperature left port liftings $\{\varphi_{\Gamma_i \to \hat{\Omega}_i}(\phi_n)\}_{1 \leqslant n \leqslant N^p_T}$
for $1 \leqslant l \leqslant n_f$ do
    for $\mu \in \mathcal{P}^{\rm tr}_{\rm Re}$ do
        Compute $\mathcal{O}^{\hat{\Omega}_i}_{\Gamma_i, \Gamma_{i+1}}(\mu; \omega^l_i, \omega^l_{i+1})$
        for $\eta \in \mathcal{P}^{\rm tr}_{\rm Pr}$ do
            Compute $\theta := \mathcal{H}^{\hat{\Omega}_i}_{\Gamma_i, \Gamma_{i+1}}(\mu, \eta; \omega^l_i, \omega^l_{i+1}, \lambda^l_i)$
        end for
    end for
end for
Compute $\mathcal{R}_u = \Big\{ \mathcal{O}^{\hat{\Omega}_i}_{\Gamma_i, \Gamma_{i+1}}(\mu; \omega^l_i, \omega^{l+1}_k) - \bar{\bar{u}}_i - \sum_{n=1}^{N^p_u} \kappa^l_{i,n} \psi_{\Gamma_i \to \hat{\Omega}_i}(\chi_n) - \sum_{n=1}^{N^p_u} \kappa^l_{i+1,n} \psi_{\Gamma_{i+1} \to \hat{\Omega}_i}(\chi_n) \Big\}_{1 \leqslant l \leqslant n_f}$
Set $\tilde{\mathcal{R}}_T = \Big\{ \mathcal{H}^{\hat{\Omega}_i}_{\Gamma_i, \Gamma_{i+1}}(\mu, \eta; \omega^l_i, \omega^l_{i+1}, \lambda^l_i) \mid \mu \in \mathcal{P}^{\rm tr}_{\rm Re}, \eta \in \mathcal{P}^{\rm tr}_{\rm Pr}, 1 \leqslant l \leqslant n_f \Big\}$
Compute $\mathcal{R}_T = \Big\{ \theta - \varphi_{\Gamma_i \to \hat{\Omega}_i}(\theta|_{\Gamma_i}) - \varphi_{\Gamma_{i+1} \to \hat{\Omega}_i}(\theta|_{\Gamma_{i+1}}) \mid \theta \in \tilde{\mathcal{R}}_T \Big\}$
Compute $\hat{X}^b_{\rm ref} = \texttt{POD}(\mathcal{R}_u, \varepsilon^b_u)$
Compute $\hat{Y}^b_{\rm ref} = \texttt{POD}(\mathcal{R}_T, \varepsilon^b_T)$
Output: $\hat{X}^b_{\rm ref}$: velocity bubble space for component $i$
        $\hat{Y}^b_{\rm ref}$: temperature bubble space for component $i$
        $N^b_u$: dimension of the velocity bubble space for component $i$
        $N^b_T$: dimension of the temperature bubble space for component $i$
```

In actual practice, we use the hierarchical POD to minimize the computational effort of the bubble training. The idea is similar to that in Algorithm 2.

Remark 3 *For the temperature bubble training, an additional step is performed. We train with the target Dirichlet boundary condition at inflow. This mandatory step is only needed for archetype components that are likely to appear at the inflow end of online-assembled geometries. In riverine contexts, this step is typically performed for channels but not for bends. In our test cases, we have performed an optional step (that can be omitted) where we train outflow ends with a homogeneous Neumann boundary condition at outflow and a linear combination of port modes at inflow.*

3.3.4 Global PR-RBC Spaces

For each new system, the PR-RBC global spaces and matrices are built using the archetype port and bubble spaces. All instantiations of a given component are represented using the bubble space of the corresponding archetype component, and all ports are represented using the port space of the corresponding archetype port. For the geometry illustrated in Figure 1, we define the algebraic forms of the intermediate velocity port spaces as $\hat{\mathbf{X}}_2^p, \dots, \hat{\mathbf{X}}_M^p$, and the algebraic forms of the velocity bubble spaces as $\hat{\mathbf{X}}_1^b, \dots, \hat{\mathbf{X}}_M^b$. For $i \in \{2, \dots, M\}$, we introduce the algebraic forms of the liftings of the port space $\hat{\mathbf{X}}_i^p$ to the left and to the right components as $\mathbf{\Psi}_i^{p,1}$ and $\mathbf{\Psi}_i^{p,2}$ respectively. The rows of these matrices correspond to local velocity FE degrees of freedom, and their columns correspond to PR-RBC velocity modes. Hence, the algebraic form of the global velocity PR-RBC basis is

$$\begin{pmatrix}
\hat{\mathbf{X}}_1^b & \mathbf{\Psi}_2^{p,1} & \mathbf{0} & \dots & & & \\
\mathbf{0} & \hat{\mathbf{X}}_2^p & \mathbf{0} & & & & \\
\mathbf{0} & \mathbf{\Psi}_2^{p,2} & \hat{\mathbf{X}}_2^b & & & & \\
\vdots & & & \ddots & & & \\
 & & & & \hat{\mathbf{X}}_{M-1}^b & \mathbf{\Psi}_M^{p,1} & \mathbf{0} \\
 & & & & \mathbf{0} & \hat{\mathbf{X}}_M^p & \mathbf{0} \\
 & & & & \mathbf{0} & \mathbf{\Psi}_M^{p,2} & \hat{\mathbf{X}}_M^b
\end{pmatrix} \in \mathbb{R}^{\mathcal{N}_u \times N_u}. \tag{87}$$

Note that the system inflow and outflow ports do not appear in the global velocity PR-RBC matrix thanks to the use of the constant contribution $\bar{\bar{\mathbf{u}}}$. We also define the algebraic forms of the non-system inflow temperature port spaces as $\hat{\mathbf{Y}}_2^p, \dots, \hat{\mathbf{Y}}_M^p, \hat{\mathbf{Y}}_{M+1}^p$, and the algebraic forms of the temperature bubble spaces as $\hat{\mathbf{Y}}_1^b, \dots, \hat{\mathbf{Y}}_M^b$. For $i \in \{2, \dots, M+1\}$, the algebraic forms of the liftings of the port space $\hat{\mathbf{Y}}_i^p$ to the left and/or to the right components are denoted $\mathbf{\Phi}_i^{p,1}$ and $\mathbf{\Phi}_i^{p,2}$ respectively. The rows of these matrices correspond to local temperature FE degrees of freedom, and their columns correspond to PR-RBC temperature modes. Hence, the algebraic form of the global temperature PR-RBC basis is

$$\begin{pmatrix}
\hat{\mathbf{Y}}_1^b & \mathbf{\Phi}_2^{p,1} & \mathbf{0} & \dots & & & & \\
\mathbf{0} & \hat{\mathbf{Y}}_2^p & \mathbf{0} & & & & & \\
\mathbf{0} & \mathbf{\Phi}_2^{p,2} & \hat{\mathbf{Y}}_2^b & & & & & \\
\vdots & & & \ddots & & & & \\
 & & & & \hat{\mathbf{Y}}_{M-1}^b & \mathbf{\Phi}_M^{p,1} & \mathbf{0} & \\
 & & & & \mathbf{0} & \hat{\mathbf{Y}}_M^p & \mathbf{0} & \\
 & & & & \mathbf{0} & \mathbf{\Phi}_M^{p,2} & \hat{\mathbf{Y}}_M^b & \mathbf{\Phi}_{M+1}^{p,1} \\
 & & & & & & \mathbf{0} & \hat{\mathbf{Y}}_{M+1}^p
\end{pmatrix} \in \mathbb{R}^{\mathcal{N}_T \times N_T}. \tag{88}$$

Here, only the system inflow port does not appear in the global temperature PR-RBC matrix thanks to the use of the lifting of the boundary condition $\mathbf{t}_{\mathrm{dir}}$. Were we to have a Dirichlet outflow boundary condition for the system, the algebraic form of the global temperature PR-RBC basis would have had the same form as for the velocity.

Let us now address the assembly of the matrices and vectors of the system. As an example, we present the assembly of the velocity stiffness matrix $\hat{\mathbf{K}}^u$. All other quantities are derived similarly. For each instantiated component Ω_i, with $i \in \{1, \ldots, M\}$, we introduce the local offline-computed reduced stiffness matrix $\hat{\mathbf{K}}_i^u$ defined as

$$\begin{aligned}
\hat{\mathbf{K}}_1^u &= \begin{pmatrix} \hat{\mathbf{X}}_1^b & \mathbf{\Psi}_2^{p,1} \end{pmatrix}^T \mathbf{K}_1^u \begin{pmatrix} \hat{\mathbf{X}}_1^b & \mathbf{\Psi}_2^{p,1} \end{pmatrix}, \\
\hat{\mathbf{K}}_i^u &= \begin{pmatrix} \mathbf{\Psi}_i^{p,2} & \hat{\mathbf{X}}_i^b & \mathbf{\Psi}_{i+1}^{p,1} \end{pmatrix}^T \mathbf{K}_i^u \begin{pmatrix} \mathbf{\Psi}_i^{p,2} & \hat{\mathbf{X}}_i^b & \mathbf{\Psi}_{i+1}^{p,1} \end{pmatrix}, \qquad \forall i \in \{2, \ldots, M-1\}, \\
\hat{\mathbf{K}}_M^u &= \begin{pmatrix} \mathbf{\Psi}_M^{p,2} & \hat{\mathbf{X}}_M^b \end{pmatrix}^T \mathbf{K}_M^u \begin{pmatrix} \mathbf{\Psi}_M^{p,2} & \hat{\mathbf{X}}_M^b \end{pmatrix}.
\end{aligned} \tag{89}$$

The global online-assembled PR-RBC stiffness matrix reads

$$\hat{\mathbf{K}}^u = \begin{pmatrix} \hat{\mathbf{K}}_1^u & \mathbf{0} & \cdots & \cdots & \mathbf{0} \\ \mathbf{0} & \hat{\mathbf{K}}_2^u & \mathbf{0} & & \vdots \\ \vdots & \ddots & \ddots & \ddots & \vdots \\ \vdots & & & \ddots & \mathbf{0} \\ \mathbf{0} & \cdots & & \mathbf{0} & \hat{\mathbf{K}}_M^u \end{pmatrix} \in \mathbb{R}^{N_u \times N_u}. \tag{90}$$

The matrices and vectors of the global system consist of as many sub-blocks as the number of instantiated components.

Matrix sparsity: The PR-RBC Newton update equation shares the block sparsity structure of the original FE equations. In fact, port degrees of freedom associated with a component are coupled only to bubble degrees of freedom associated with neighboring components; and bubble degrees of freedom in any component are coupled only to port and bubble degrees of freedom associated with that component. Most importantly, the PR-BRC Newton update matrix has many fewer degrees of freedom compared to the FE Newton update matrix thanks to port reduction and bubble reduction.

The component-based method makes it possible to reduce offline learning to a few inexpensive archetype components and ports which characterize the geometry of the system. The major interest of the PR-RBC method in comparison with standard RB methods lies in the capacity of a single offline reduction to analyze any new system synthesized from a library of generic components initially determined. The archetype components are then instantiated as subdomains to form any given model in a family of problems. Since the archetype components are typically parametrized, the family of problems associated with a given library (i.e., the set of models which can be formed from assemblies of instantiated components) can be very large. The component-to-model assembly process is described in detail in the acoustics context in [16] and in the structural context in [37].

We also note that a library can expand over time, with incremental port training and subsequent bubble training to accommodate new components.

We summarize the important role of components. First, regarding parametrization, components allow for the reduction a single large problem with many model parameters to many small problems with just a few local parameters. We thus address, by dividing and conquering, the curse of dimensionality which often plagues reduced basis techniques. However, we do not address local parameterization in this paper. Second, components permit the development of local approximation spaces over each archetype component, which offer flexibility and ultimately computational efficiency. In particular, components facilitate models in which the topology may vary as a function of the parameter. Third, in the offline stage, we solve FE problems only over pairs of components (port training) or single components (bubble training); we never solve FE problems for entire systems. We may thus consider large models, and in particular models which may be too large to admit global FE solutions. Fourth, we may amortize our offline effort not over just a particular model — in the real-time and multi-query limits per usual reduced basis justification — but over all models which we can and may synthesize from the library of archetype components. We can thus tolerate higher offline costs. In fact, a common impediment to model order reduction without components is the relative inflexibility imposed by *a priori* specification of a particular problem and model parameter domain. Fifth, and finally, we facilitate the development of new models in particular by engineers without knowledge of the underlying numerical approaches.

4 Numerical Results

In this section, we illustrate the above developments for two-dimensional rivers. Consider a library of 4 archetype components: a straight channel, an island, a bend, and a flipped bend, all illustrated in Figure 4. Our goal is to apply the PR-RBC method to the steady state Navier-Stokes equation (4) supplemented by the passive scalar equation (5). Regarding space discretization, we recall that we use P2-bubble finite elements for the velocity field, P1-discontinuous finite elements for the pressure field, and P2 finite elements for the temperature field. The number of degrees of freedom for the velocity and the temperature on ports and bubbles is given in Table 1. The parametrization is similar for both test cases since they share the same archetype components. The Reynolds number μ varies in the interval $\mathcal{P}_{\rm Re} = [10, 15]$ and the Prandtl number η varies in the interval $\mathcal{P}_{\rm Pr} = [1, 6]$. For parameter sampling, we will use the following discrete training sets: $\mathcal{P}^{\rm tr}_{\rm Re,1} = \{i \mid 10 \leqslant i \leqslant 15\}$, $\mathcal{P}^{\rm tr}_{\rm Re,2} = \{i/2 \mid 20 \leqslant i \leqslant 30\}$, $\mathcal{P}^{\rm tr}_{\rm Pr,1} = \{i \mid 1 \leqslant i \leqslant 6\}$, $\mathcal{P}^{\rm tr}_{\rm Pr,2} = \{i/2 \mid 2 \leqslant i \leqslant 12\}$. We will also use the verification sets $\mathcal{P}^{\rm ver}_{\rm Re} = \{i/4 \mid 40 \leqslant i \leqslant 60\}$ and $\mathcal{P}^{\rm ver}_{\rm Pr} = \{i/4 \mid 4 \leqslant i \leqslant 24\}$ for online assessment. The verification sets have been derived by uniform sampling of the training set. They have proved

Archetype components	ports	island	bend	channel	flipped bend
Velocity degrees of freedom	62	5668	3750	4686	3726
Temperature degrees of freedom	31	1920	1272	1587	1264

Table 1: Test cases (a) and (b) - FE degrees of freedom.

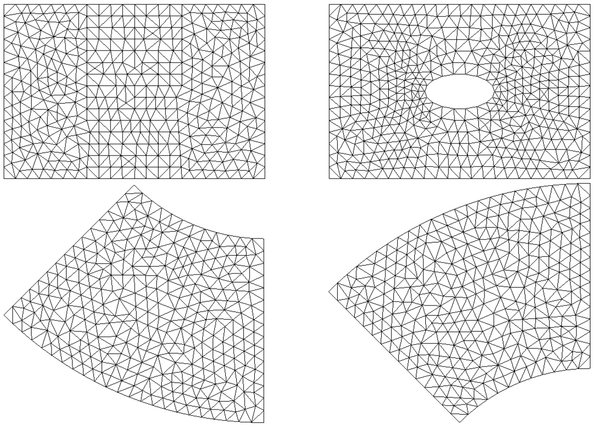

Figure 4: Test cases (a) and (b) - Meshes of the archetype components. Top left: Straight channel. Top right: Island. Bottom left: Bend. Bottom right: Flipped bend.

useful during our tests to compare the performance of the PR-RBC model with the FE model. For the velocity port training algorithm 2, we use $R = 5$, where R is the number of zero-flowrate basis functions used in (61). For the temperature port training, we use forcing functions of the form $\sum_{i=1}^{5} o_i \cos(i\pi y)$, where o_i are random coefficients generated using a normal distribution of mean 0 and variance 1. Other sampling strategies can be used as long as they have sufficient data points that are not part of the training sets. Regarding implementation, the FE computations use `FreeFem++` [38] and the PR-RBC algorithms have been developed in `Python`.

4.1 Test Case (a): Straight River

Our first test case is a straight 'river' (or channel), formed using five instantiations of elements from the library of archetype components. Using the notation in (4), $\partial\Omega^{\text{cavity}}$ is the boundary of the inner cavity in the island components. The assembled geometry is illustrated in Figure 5. The final mesh has $\mathcal{N}_u = 25146$ velocity degrees of freedom and $\mathcal{N}_T = 8477$ temperature degrees of freedom. In Figure 6, we show the FE velocity and temperature profiles over the the straight river for two different parameter pairs. Overall, the system outflow temperature increases as the Reynolds number μ and the Prandtl number η increase. Furthermore, the convective effects are more apparent for larger values of η.

We assess the performance of our method for the steady state Navier-Stokes equation and the passive scalar equation. We first describe the offline stage (cf. algorithms 2 and the distributed version of 3). In a first configuration, we use the training sets $\mathcal{P}^{\text{tr}}_{\text{Re},1}$ and $\mathcal{P}^{\text{tr}}_{\text{Pr},1}$, and a number of forcing functions $n_f = 4$. We recall that n_f is the number of random functions generated for training ports and bubbles. It is the number of functions generated at the forcing ports of component pairs or single components. The value of n_f will be increased in Test case (b). For $\varepsilon^p_u = \varepsilon^p_T = 10^{-3}$, we

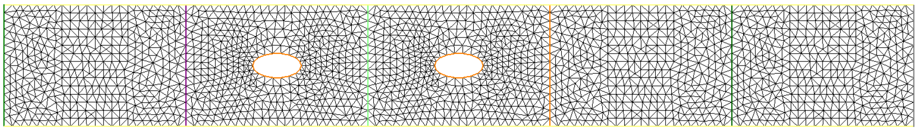

Figure 5: Test case (a) - Mesh of a 5-component straight river with $\mathcal{N}_u = 25146$ and $\mathcal{N}_T = 8477$.

.

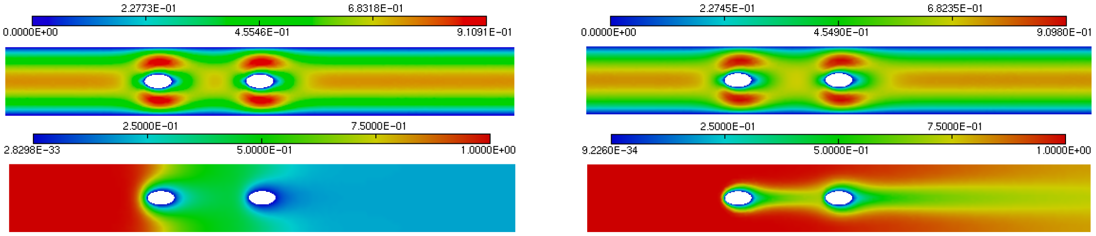

Figure 6: Test case (a) - FE solutions. Left: For $(\mu, \eta) = (10, 1)$. Right: For $(\mu, \eta) = (15, 6)$. Top: Velocity field. Bottom: Temperature field.

obtain a velocity port basis of cardinality $N_u^p = 10$ and a temperature port basis of cardinality $N_T^p = 5$. The first port modes for the velocity training are illustrated in Figure 7. As can be conjectured from visual inspection, the curves in the left panel of Figure 7 satisfy the zero-flowrate criterion (i.e., a vanishing integral over $[-1, 1]$). Using the collected port modes, we perform the bubble training with $\varepsilon_u^b = \varepsilon_T^b = 10^{-3}$. We obtain $N_u^i = 13$, $N_u^b = 15$, $N_u^c = 16$, and $N_u^{fb} = 15$ velocity bubble modes, where the superscripts indicate the component initials, i.e., $i \equiv$ island, $b \equiv$ bend, $c \equiv$ channel, and $fb \equiv$ flipped bend. Regarding the temperature training, we obtain $N_T^i = 12$, $N_T^b = 17$, $N_T^c = 1$, and $N_T^{fb} = 18$ temperature bubble modes. The first velocity bubble modes are illustrated in Figure 8 and the first temperature bubble modes are illustrated in Figure 9. We infer from visual inspection that zero-flowrate is satisfied for the velocity bubble modes, and natural boundary conditions on the walls, and homogeneous Dirichlet on the cavity are satisfied for the temperature bubble modes. Moreover, the cardinalities of the reduced basis spaces for the velocity and for the temperature are shown in Tables 2 and 3 respectively. One can notice that the channel archetype component only needs a single bubble mode to represent the temperature PR-RBC solution field for $\varepsilon_u^b = \varepsilon_u^b = \varepsilon_T^b = \varepsilon_T^b = 10^{-3}$, which corroborates the advantage of using domain decomposition to represent solution fields for systems with recurring geometry patterns. For the velocity training, the cardinalities of the port and bubble spaces all increase as tolerances are tightened up to $\varepsilon_u^p = \varepsilon_u^b = 10^{-5}$. Afterwards, the increase in the number of velocity port modes continues, and a stagnation in the number of velocity bubble modes is observed. This phenomenon is due to the fact that all the energy in the set of collected snapshots during the offline random training is already included in the chosen POD modes. Note that the increase in the number of

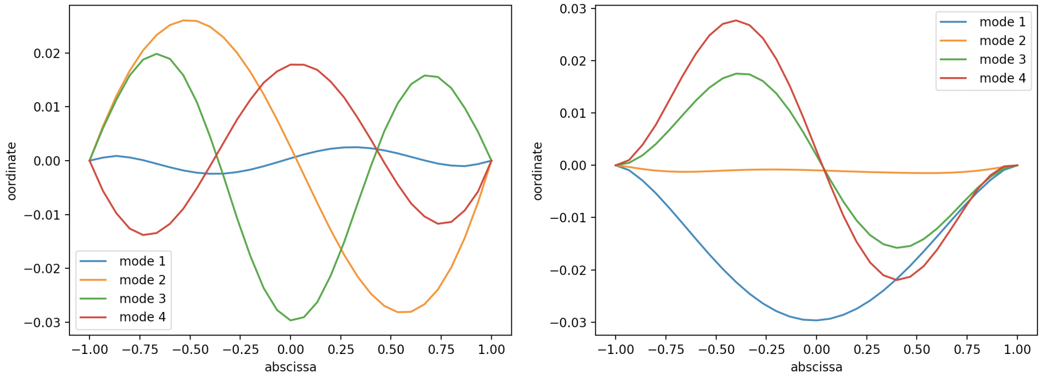

Figure 7: Test case (a) - First velocity port modes for $\varepsilon_T^p = 10^{-3}$, $n_f = 4$, and $\mathcal{P}_{\mathrm{Re},1}^{\mathrm{tr}}$. Left: Modes in the normal direction (with regard to the interface ports). Right: Modes in the tangential direction.

port modes beyond the stagnation threshold for the bubbles highlights the importance of the port representation in rendering the behavior of the solution field through the port interfaces. A similar trend is observed for the temperature with a stagnation threshold $\varepsilon_u^b = \varepsilon_u^b = \varepsilon_T^b = \varepsilon_T^b = 10^{-7}$ for the bubbles. The number of temperature port modes also stagnates at $\varepsilon_u^b = \varepsilon_u^b = \varepsilon_T^b = \varepsilon_T^b = 10^{-5}$.

ε	N_u^p	N_u^i	N_u^b	N_u^c	N_u^{fb}	N_u	γ_{N_u}/β_{N_u}	PR-RBC error	best-fit error	condition number
10^{-2}	5	7	7	8	7	58	1.9×10^2	6.5×10^{-2}	6.3×10^{-2}	$1.3 \times 10^2 - 1.4 \times 10^2$
10^{-3}	10	13	15	16	15	114	2.1×10^2	1.4×10^{-2}	1.3×10^{-2}	$1.5 \times 10^2 - 1.5 \times 10^2$
10^{-4}	14	22	23	24	24	172	2.2×10^2	5.4×10^{-3}	5.2×10^{-3}	$1.6 \times 10^2 - 1.6 \times 10^2$
10^{-5}	28	24	24	24	24	232	2.3×10^2	3.6×10^{-3}	3.4×10^{-3}	$1.7 \times 10^2 - 1.7 \times 10^2$
10^{-6}	43	24	24	24	24	292	2.4×10^2	4.0×10^{-3}	2.8×10^{-3}	$1.7 \times 10^2 - 1.8 \times 10^2$
10^{-7}	43	24	24	24	24	292	2.4×10^2	6.8×10^{-3}	5.8×10^{-3}	$1.7 \times 10^2 - 1.8 \times 10^2$
10^{-9}	44	24	24	24	24	296	2.4×10^2	4.7×10^{-3}	2.7×10^{-3}	$1.8 \times 10^2 - 1.9 \times 10^2$

Table 2: Test case (a) - For $n_f = 4$, $\mathcal{P}_{\mathrm{Re},1}^{\mathrm{tr}}$, and $\varepsilon = \varepsilon_u^p = \varepsilon_u^b$. Left: Offline cardinalities of the velocity PR-RBC spaces (valid for test cases (a) and (b)). Right: Online quantities.

We next discuss the online stage, we first assemble the constant velocity contribution $\bar{\bar{u}}$ and the Dirichlet temperature lifting T_{dir} for the entire system as illustrated in the top panels of Figures (10) and (11) respectively. We also assemble the global PR-RBC basis and the global PR-RBC matrices and vectors of the reduced systems (35) and (45). The sparsity of the velocity stiffness matrix and that of the PR-RBC basis are illustrated in Figure 12. The matrices are block μ–diagonal and port and bubble degrees of freedom are only coupled to port and bubble degrees of freedom of neighboring components. Hence, the matrices of the PR-RBC system are sparse and the solution cost is cheaper than for standard RB methods where online matrices are dense. We can then solve for the PR-RBC velocity contribution $\hat{u}(\mu) - \bar{\bar{u}}$ and the PR-RBC temperature contribution $\hat{T}(\mu, \eta) - T_{\mathrm{dir}}$. These fields are illustrated in the bottom panels of Figures (10) and (11) for $\mu = 15$ and $\eta = 6$, with

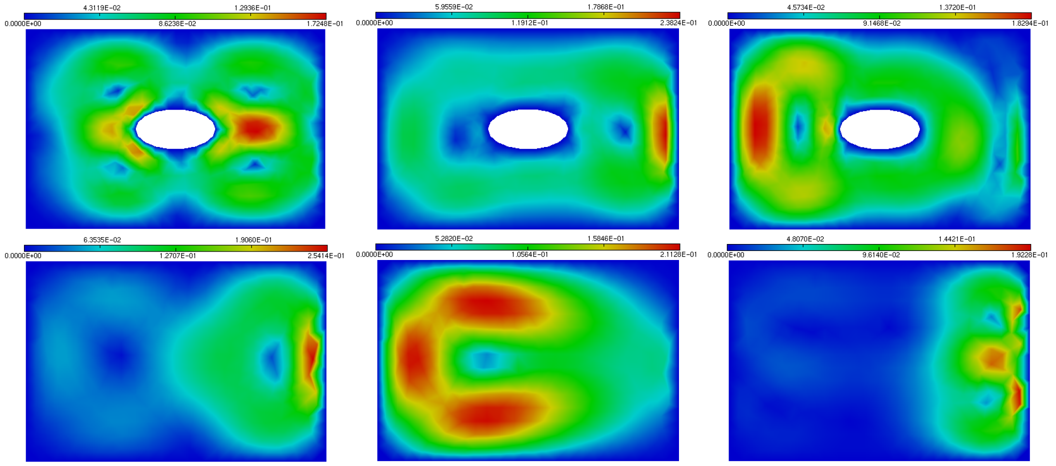

Figure 8: Test cases (a) and (b) - First velocity bubble modes (norm) for $\varepsilon_u^b = 10^{-3}$, $n_f = 4$, and $\mathcal{P}^{\text{tr}}_{\text{Re},1}$. Top: For the island archetype component. Bottom: For the channel archetype component.

ε	N_T^p	N_T^i	N_T^b	N_T^c	N_T^{fb}	N_T	PR-RBC error	best-fit error	condition number
10^{-2}	3	4	6	1	6	26	6.1×10^{-1}	3.7×10^{-1}	$2.7 \times 10^2 - 7.8 \times 10^2$
10^{-3}	5	12	17	1	18	52	3.7×10^{-1}	2.1×10^{-1}	$3.7 \times 10^2 - 1.4 \times 10^3$
10^{-4}	9	30	29	4	30	117	6.8×10^{-2}	4.8×10^{-2}	$4.7 \times 10^2 - 8.6 \times 10^2$
10^{-5}	10	57	29	9	29	191	2.1×10^{-2}	1.4×10^{-2}	$5.0 \times 10^2 - 7.9 \times 10^2$
10^{-6}	10	94	28	24	29	310	8.0×10^{-3}	2.5×10^{-3}	$6.6 \times 10^2 - 1.0 \times 10^3$
10^{-7}	10	129	28	34	32	410	7.6×10^{-3}	1.2×10^{-3}	$7.6 \times 10^2 - 1.2 \times 10^3$
10^{-9}	10	127	28	33	30	403	7.6×10^{-3}	1.0×10^{-3}	$7.6 \times 10^2 - 1.3 \times 10^3$

Table 3: Test case (a) - For $n_f = 4$, $\mathcal{P}^{\text{tr}}_{\text{Re},1}$, $\mathcal{P}^{\text{tr}}_{\text{Pr},1}$, and $\varepsilon = \varepsilon_u^p = \varepsilon_u^b = \varepsilon_T^p = \varepsilon_T^b$. Left: Offline cardinalities of the temperature PR-RBC spaces (valid for test cases (a) and (b)). Right: Online quantities.

$n_f = 4$, $\mathcal{P}^{\text{tr}}_{\text{Re},1}$, $\mathcal{P}^{\text{tr}}_{\text{Pr},1}$, and $\varepsilon_u^p = \varepsilon_u^b = \varepsilon_T^p = \varepsilon_T^b = 10^{-5}$. For each solution field, the sum of the Dirichlet lifting T_{dir} (15) and the PR-RBC contribution yields the final PR-RBC solution.

In order to investigate the performance of the method, we run the online stage for several values of the POD truncation thresholds using the verification sets $\mathcal{P}^{\text{ver}}_{\text{Re}}$ and $\mathcal{P}^{\text{ver}}_{\text{Pr}}$. The condition numbers of the online PR-RBC systems and the relative H^1-errors for the velocity and the temperature are shown in the convergence Tables 2 and 3 respectively. We recall that β and γ are respectively the stability and continuity constants introduced in (49) and (51). Overall, the PR-RBC systems are not ill-conditioned and the accuracy improves with richer velocity and temperature spaces. However, we highlight that some non-monotonicity can be observed for close tolerances. In fact, the randomized training procedures produce non-nested (or non-hierarchical) spaces. This is confirmed with the non-monotonicity not only of the PR-RBC error, but also of the best-fit error (53) in the last rows of Table 2. In particular, the tolerances $\varepsilon_u^p = \varepsilon_u^b = 10^{-6}$ and $\varepsilon_u^p = \varepsilon_u^b = 10^{-7}$ in Table 2 produce the

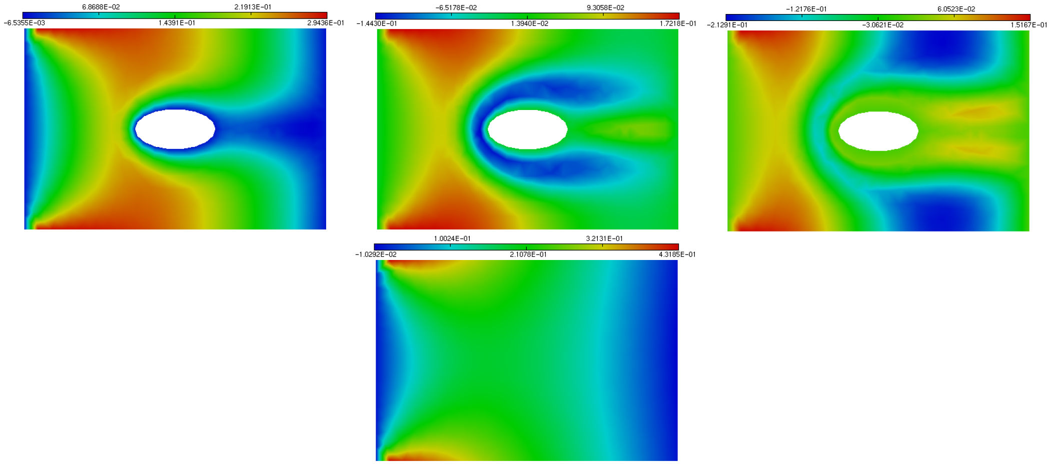

Figure 9: Test cases (a) and (b) - First temperature bubble modes for $\varepsilon_T^b = 10^{-3}$, $n_f = 4$, and $\mathcal{P}^{\mathrm{tr}}_{\mathrm{Pr},1}$. Top: For the island archetype component. Bottom: For the channel archetype component.

same number of modes, for the ports and for every bubble archetype component. Yet, the errors are slightly different due to the randomization of the offline training. Finally, along with the PR-RBC errors and the best-fit errors, the value of γ_{N_u}/β_{N_u} in Table 2 shows that the Caloz-Raviart *a priori* error estimate in (52) is satisfied for all tolerances.

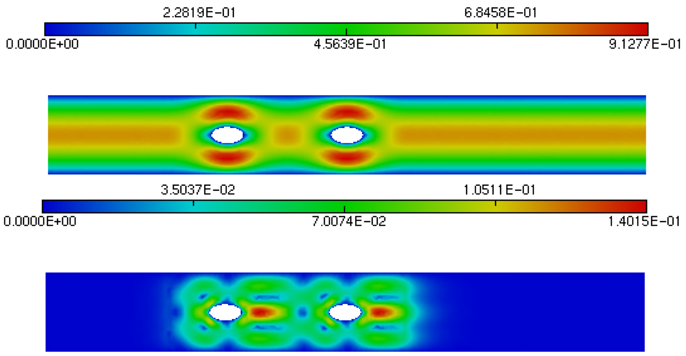

Figure 10: Test case (a) - Top: $\bar{\bar{u}}$. Bottom: PR-RBC velocity contribution $\hat{u}(\mu) - \bar{\bar{u}}$ for $\mu = 15$, with $n_f = 4$, $\mathcal{P}^{\mathrm{tr}}_{\mathrm{Re},1}$ and $\varepsilon^p_u = \varepsilon^b_u = 10^{-5}$.

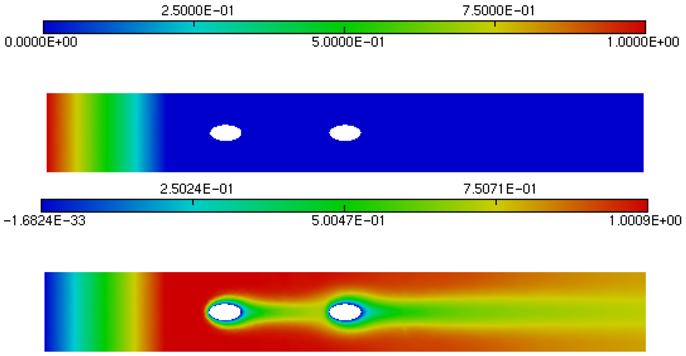

Figure 11: Test case (a) - Top: Dirichlet lifting T_{dir}. Bottom: PR-RBC temperature contribution $\hat{T}(\mu,\eta) - T_{\mathrm{dir}}$ for $(\mu,\eta) = (15,6)$, with $n_f = 4$, $\mathcal{P}^{\mathrm{tr}}_{\mathrm{Re},1}$, $\mathcal{P}^{\mathrm{tr}}_{\mathrm{Pr},1}$, and $\varepsilon^p_u = \varepsilon^b_u = \varepsilon^p_T = \varepsilon^b_T = 10^{-5}$.

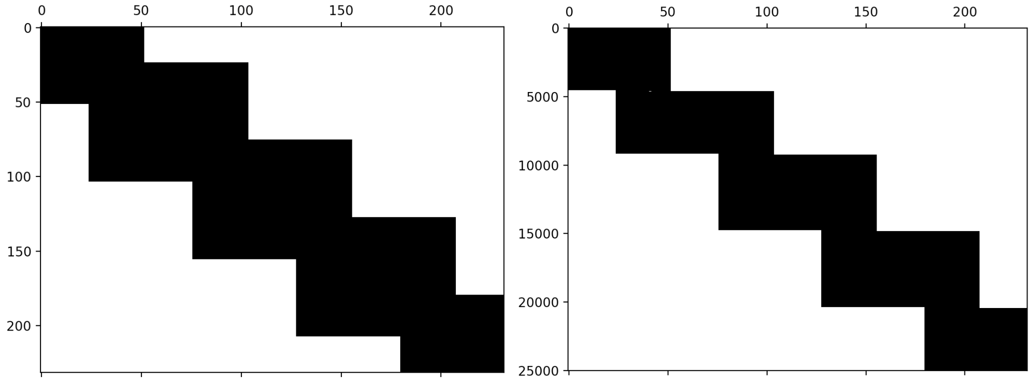

Figure 12: Test case (a) - Sparsity of the global velocity matrices for $\varepsilon_u^p = \varepsilon_u^b = 10^{-5}$. Left: Velocity stiffness matrix $\hat{\mathbf{K}}^u$. Right: Global velocity PR-RBC basis $\hat{\mathbf{X}}$.

4.2 Test Case (b): Seine-like River

A major advantage of the PR-RBC is that new systems and geometries can be considered in the online stage. For this test case, we assemble 17 component instantiations to form the mesh of a river illustrated in Figure 13. The geometry is inspired from the Parisian fragment of the Seine River, starting from the south-eastern 'Bois de Vincennes' towards the south-western 'Bois de Boulogne'. The final mesh has $\mathcal{N}_u = 77824$ velocity degrees of freedom and $\mathcal{N}_T = 26206$ temperature degrees of freedom. In this test case, one can notice that some of the ports are rotated. Such rotations also occur during the offline training for pairs of components whose right archetype component is either a bend or a flipped bend. Thus, the training for the library of components in Figure 4 uses rotation operators to adapt the input functions in (61) on the left ports of the bend and the flipped bend for the velocity field. Additionally, rotations are used during the online stage for all online-built systems featuring a bend or a flipped bend. These rotations are required to correctly represent the port and bubble velocity modes, and to assemble the final PR-RBC velocity solution field. Conversely, the temperature solution field is scalar and does not require such adjustments.

For $n_f = 4$, $\mathcal{P}^{\mathrm{tr}}_{\mathrm{Re},1}$, and $\mathcal{P}^{\mathrm{tr}}_{\mathrm{Pr},1}$, the offline stage has already been performed (cf. test case (a)). Hence, the cardinalities of the PR-RBC velocity and temperature spaces are the same listed earlier in Tables 2 and 3. We also perform a more extensive training with a number of forcing functions $n_f = 8$, and the training sets $\mathcal{P}^{\mathrm{tr}}_{\mathrm{Re},2}$ and $\mathcal{P}^{\mathrm{tr}}_{\mathrm{Pr},2}$. The cardinalities of the PR-RBC velocity and temperature spaces are given in Tables 4 and 5 respectively. The trends are the same as described for test case (a). Besides, we notice that the bubble spaces for all archetype components have more modes for both the velocity and the temperature. Tables 4 and 5 also list the number of final

ε	N_u^p	N_u^i	N_u^b	N_c^b	N_u^{fb}	N	γ_{N_u}/β_{N_u}	PR-RBC error	best-fit error	condition number
10^{-3}	10	15	16	17	16	439	2.2×10^2	6.6×10^{-3}	6.5×10^{-3}	$1.6 \times 10^2 - 1.6 \times 10^2$
10^{-4}	14	28	29	31	30	736	2.4×10^2	1.7×10^{-3}	1.6×10^{-3}	$1.7 \times 10^2 - 1.8 \times 10^2$
10^{-5}	29	48	54	56	52	1380	2.5×10^2	4.5×10^{-4}	3.3×10^{-4}	$1.8 \times 10^2 - 1.9 \times 10^2$
10^{-6}	44	79	75	77	75	2011	2.6×10^2	2.7×10^{-3}	1.2×10^{-4}	$1.9 \times 10^2 - 2.1 \times 10^2$
10^{-7}	44	81	77	77	75	2021	2.6×10^2	2.8×10^{-3}	1.2×10^{-4}	$1.9 \times 10^2 - 2.1 \times 10^2$
10^{-9}	45	82	75	77	74	2034	2.6×10^2	3.1×10^{-3}	1.3×10^{-4}	$1.9 \times 10^2 - 2.1 \times 10^2$

Table 4: Test case (b) - For $n_f = 8$, $\mathcal{P}^{\mathrm{tr}}_{\mathrm{Re},2}$, and $\varepsilon = \varepsilon_u^p = \varepsilon_u^b$. Left: Offline cardinalities of the velocity PR-RBC spaces (valid for test cases (a) and (b)). Right: Online quantities.

ε	N_T^p	N_T^i	N_T^b	N_T^c	N_T^{fb}	N_T	PR-RBC error	best-fit error	condition number
10^{-3}	5	12	18	2	18	213	2.1×10^{-1}	1.0×10^{-1}	$1.3 \times 10^3 - 2.5 \times 10^3$
10^{-4}	9	30	38	4	38	435	6.5×10^{-2}	3.6×10^{-2}	$1.4 \times 10^3 - 2.2 \times 10^3$
10^{-5}	10	63	39	9	39	605	4.1×10^{-2}	9.3×10^{-3}	$1.4 \times 10^3 - 2.2 \times 10^3$
10^{-6}	10	105	39	24	38	879	4.0×10^{-2}	2.3×10^{-3}	$1.5 \times 10^3 - 2.5 \times 10^3$
10^{-7}	10	170	39	44	38	1274	4.0×10^{-2}	9.1×10^{-4}	$1.8 \times 10^3 - 2.9 \times 10^3$
10^{-9}	10	193	40	43	39	1337	4.0×10^{-2}	7.7×10^{-4}	$1.7 \times 10^3 - 2.9 \times 10^3$

Table 5: Test case (b) - For $n_f = 8$, $\mathcal{P}^{\mathrm{tr}}_{\mathrm{Re},2}$, $\mathcal{P}^{\mathrm{tr}}_{\mathrm{Pr},2}$, and $\varepsilon = \varepsilon_u^p = \varepsilon_u^b = \varepsilon_T^p = \varepsilon_T^b$. Left: Offline cardinalities of the temperature PR-RBC spaces (valid for test cases (a) and (b)). Right: Online quantities.

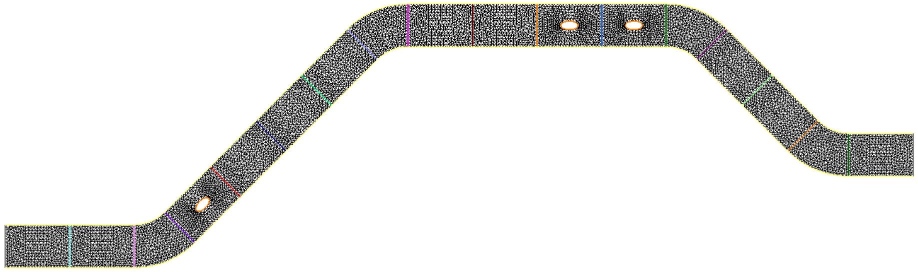

Figure 13: Test case (b) - Mesh of a 17-component Seine-like river with $\mathcal{N}_u = 77824$ and $\mathcal{N}_T = 26206$.

PR-RBC velocity modes N_u and temperature modes N_T for the entire Seine-like river. We observe that the number of final modes is far larger than for the straight river in test case (a) (cf. Tables 2 and 3). The more the components, the larger the PR-RBC spaces. However, the number of PR-RBC modes remains negligible compared to the number of FE degrees of freedom. As POD tolerances are tightened, one can notice a stagnation of the velocity best-fit error (cf. Table 4). Furthermore, the comparison of the PR-RBC errors in Table 6 for different values of n_f and different choices of the training sets shows that the more extensive the training, the lower the error. Also, the non-monotonicity previously observed in Test case (a) with $n_f = 4$ at $\varepsilon = 10^{-6}$ (cf. Table 2) for the PR-RBC error also arises for this test case. This can be explained by the upper bound in (52), which is corroborated by the values of γ_{N_u}/β_{N_u}. More importantly, comparing the PR-RBC and the best-fit errors in Table 6 suggests that we get convergence for the POD. We can then infer that the saturation in the best-fit error (and consequently in the PR-RBC error) with tighter tolerances is because n_f and $\mathcal{P}^{\text{tr}}_{\text{Re}}$ are the limiting factors. Once increased, one can expect the errors to decrease further. Besides, we highlight that it is expected that the PR-RBC error ranges for the temperature field can be higher than for the velocity field as can be observed in Table 7. In fact, the passive scalar equation takes the velocity field as an input and any approximation error for the velocity field propagates to the temperature field. This test case is more complex and the presence of bends and islands leads to more inertial effects in the velocity field and more convective effects in the temperature field. Nonetheless, the PR-RBC model still proves accurate as corroborated by the convergence data in Tables 6 and 7. Finally, figures 14 and 15 display the online-computed PR-RBC velocity and temperature solution fields for a Reynolds number $\mu = 15$ and a Prandtl number $\eta = 6$, with a number of forcing functions $n_f = 4$, training sets $\mathcal{P}^{\text{tr}}_{\text{Re},1}$ and $\mathcal{P}^{\text{tr}}_{\text{Pr},1}$, and tolerances $\varepsilon^p_u = \varepsilon^b_u = \varepsilon^p_T = \varepsilon^b_T = 10^{-5}$.

Regarding online efficiency, the mean execution time is reported in Table 8. Note that small execution times are upper bounds of the effective runtime due to other processes running on a computer. In RB methods, a standard efficiency indicator is an RB execution time that is preferably around or less than 5% of the FE computation time. We infer from Table 8 that it is the case for both a loose and a tight POD truncation threshold.

ε	PR-RBC error		best-fit error	
	$n_f = 4$, $\mathcal{P}^{\mathrm{tr}}_{\mathrm{Re},1}$	$n_f = 8$, $\mathcal{P}^{\mathrm{tr}}_{\mathrm{Re},2}$	$n_f = 4$, $\mathcal{P}^{\mathrm{tr}}_{\mathrm{Re},1}$	$n_f = 8$, $\mathcal{P}^{\mathrm{tr}}_{\mathrm{Re},2}$
$10^{-3}/10^{-3}$	1.3×10^{-2}	6.6×10^{-3}	1.2×10^{-2}	6.5×10^{-3}
$10^{-4}/10^{-4}$	5.1×10^{-3}	1.7×10^{-3}	4.9×10^{-3}	1.6×10^{-3}
$10^{-5}/10^{-5}$	4.1×10^{-3}	4.5×10^{-4}	3.9×10^{-3}	3.3×10^{-4}
$10^{-6}/10^{-6}$	4.1×10^{-3}	2.7×10^{-3}	3.3×10^{-3}	1.2×10^{-4}
$10^{-7}/10^{-7}$	6.6×10^{-3}	2.8×10^{-3}	5.7×10^{-3}	1.2×10^{-4}
$10^{-9}/10^{-9}$	4.3×10^{-3}	3.1×10^{-3}	2.9×10^{-3}	1.3×10^{-4}

Table 6: Test case (b) - Comparison of velocity convergence quantities with $\varepsilon = \varepsilon^p_u = \varepsilon^b_u$.

ε	PR-RBC error		best-fit error	
	$n_f = 4$, $\mathcal{P}^{\mathrm{tr}}_{\mathrm{Re},1}$, $\mathcal{P}^{\mathrm{tr}}_{\mathrm{Pr},1}$	$n_f = 8$, $\mathcal{P}^{\mathrm{tr}}_{\mathrm{Re},2}$, $\mathcal{P}^{\mathrm{tr}}_{\mathrm{Pr},2}$	$n_f = 4$, $\mathcal{P}^{\mathrm{tr}}_{\mathrm{Re},1}$, $\mathcal{P}^{\mathrm{tr}}_{\mathrm{Pr},1}$	$n_f = 8$, $\mathcal{P}^{\mathrm{tr}}_{\mathrm{Re},2}$, $\mathcal{P}^{\mathrm{tr}}_{\mathrm{Pr},2}$
10^{-3}	3.2×10^{-1}	2.1×10^{-1}	1.7×10^{-1}	1.0×10^{-1}
10^{-4}	6.9×10^{-2}	6.5×10^{-2}	4.0×10^{-2}	3.6×10^{-2}
10^{-5}	4.3×10^{-2}	4.1×10^{-2}	1.3×10^{-2}	9.3×10^{-3}
10^{-6}	4.0×10^{-2}	4.0×10^{-2}	2.4×10^{-3}	2.3×10^{-3}
10^{-7}	3.9×10^{-2}	4.0×10^{-2}	1.2×10^{-3}	9.1×10^{-4}
10^{-9}	3.9×10^{-2}	4.0×10^{-2}	1.1×10^{-3}	7.7×10^{-4}

Table 7: Test case (b) - Comparison of temperature convergence quantities with $\varepsilon = \varepsilon^p_u = \varepsilon^b_u = \varepsilon^p_T = \varepsilon^b_T$.

	FEM	RB with $\varepsilon = 10^{-3}$	RB with $\varepsilon = 10^{-5}$
Execution time in s	280	1.0	7.5

Table 8: Test case (b) - Online execution times for $n_f = 4$, $\mathcal{P}^{\mathrm{tr}}_{\mathrm{Re},1}$, $\mathcal{P}^{\mathrm{tr}}_{\mathrm{Pr},1}$.

5 Conclusion

In this paper, we have devised a new PR-RBC method for nonlinear PDEs governing fluid flows in non-forked riverine geometries and channels. The new method allows for an effective treatment of incompressibility and nonlinearity in the Navier-Stokes equation. It also suggests a suitable treatment for convective effects in the passive scalar equation. To accommodate nonlinearities, port and bubble spaces are built sequentially in a randomized manner. Moreover, the static condensation used in the linear PR-RBC method is replaced with an online stage where port and bubble degrees of freedom are coupled for neighboring components. Furthermore, we have numerically shown that this methodology builds a reliable low-dimensional model. A relevant future direction is the application of the method in combination with the EIM to address non-polynomial nonlinearities. Finally, fluid flows in forked riverine geometries are an interesting engineering application to explore.

Acknowledgements
We thank Christopher Kees (LSU) and Tristan de Lataillade (AnotherBrain) for stimulating discussions, and the MIT WCC for proofreading.

Funding
This work is funded by the ARO grant W911NF1910098, entitled ‘Parametrized Model Order Reduction for Engineered Coastal and Hydraulic Systems: Component Libraries and Digital Twins’.

Competing interests
The authors declare that they have no competing interests.

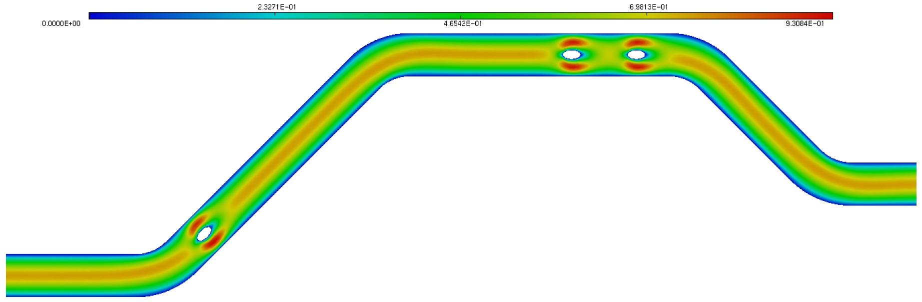

Figure 14: Test case (b) - PR-RBC velocity solution $\hat{u}(\mu)$ for $\mu = 15$, with $n_f = 4$, $\mathcal{P}^{\mathrm{tr}}_{\mathrm{Re},1}$, and $\varepsilon^p_u = \varepsilon^b_u = 10^{-5}$.

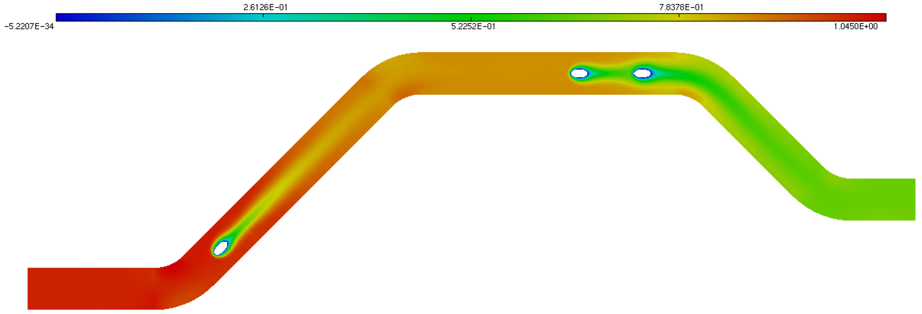

Figure 15: Test case (b) - PR-RBC temperature solution $\hat{T}(\mu, \eta)$ for $(\mu, \eta) = (15, 6)$, with $n_f = 4$, $\mathcal{P}^{\mathrm{tr}}_{\mathrm{Re},1}$, $\mathcal{P}^{\mathrm{tr}}_{\mathrm{Pr},1}$, and $\varepsilon^p_u = \varepsilon^b_u = \varepsilon^p_T = \varepsilon^b_T = 10^{-5}$.

Authors' contributions
Both authors participated in the definition of techniques and algorithms. Both authors read and approved the final manuscript.

Author details
Department of Mechanical Engineering, Massachusetts Institute of Technology, Cambridge, USA.

References

1. D. B. P. Huynh, D. J. Knezevic, and A. T. Patera, "A static condensation reduced basis element method: complex problems," Comput. Methods Appl. Mech. Engrg., vol. 259, pp. 197–216, 2013.
2. W. C. Hurty, "Dynamic analysis of structural systems using component modes," AIAA Journal, vol. 3, no. 4, pp. 678–685, 1965.
3. R. R. Craig Jr and M. C. Bampton, "Coupling of substructures for dynamic analyses.," AIAA journal, vol. 6, no. 7, pp. 1313–1319, 1968.
4. U. L. Hetmaniuk and R. B. Lehoucq, "A special finite element method based on component mode synthesis," M2AN Math. Model. Numer. Anal., vol. 44, no. 3, pp. 401–420, 2010.
5. A. K. Noor and J. M. Peters, "Reduced basis technique for nonlinear analysis of structures," AIAA journal, vol. 18, no. 4, pp. 455–462, 1980.
6. A. Quarteroni, A. Manzoni, and F. Negri, Reduced basis methods for partial differential equations: an introduction, vol. 92. Springer, 2015.
7. J. S. Hesthaven, G. Rozza, B. Stamm, et al., Certified reduced basis methods for parametrized partial differential equations, vol. 590. Springer, 2016.
8. Y. Maday and E. M. Ronquist, "The reduced basis element method: application to a thermal fin problem," SIAM Journal on Scientific Computing, vol. 26, no. 1, pp. 240–258, 2004.

9. E. L. Wilson, "The static condensation algorithm," International Journal for Numerical Methods in Engineering, vol. 8, no. 1, pp. 198–203, 1974.
10. J. L. Eftang and A. T. Patera, "Port reduction in parametrized component static condensation: approximation and a posteriori error estimation," International Journal for Numerical Methods in Engineering, vol. 96, no. 5, pp. 269–302, 2013.
11. A. Pinkus, N-widths in Approximation Theory, vol. 7. Springer Science & Business Media, 2012.
12. I. Babuska and R. Lipton, "Optimal local approximation spaces for generalized finite element methods with application to multiscale problems," Multiscale Modeling & Simulation, vol. 9, no. 1, pp. 373–406, 2011.
13. K. Smetana and A. T. Patera, "Optimal local approximation spaces for component-based static condensation procedures," SIAM J. Sci. Comput., vol. 38, no. 5, pp. A3318–A3356, 2016.
14. K. Veroy, C. Prud'Homme, D. Rovas, and A. Patera, "A posteriori error bounds for reduced-basis approximation of parametrized noncoercive and nonlinear elliptic partial differential equations," in 16th AIAA Computational Fluid Dynamics Conference, p. 3847, 2003.
15. P. Binev, A. Cohen, W. Dahmen, R. DeVore, G. Petrova, and P. Wojtaszczyk, "Convergence rates for greedy algorithms in reduced basis methods," SIAM journal on mathematical analysis, vol. 43, no. 3, pp. 1457–1472, 2011.
16. J. Ballani, P. Huynh, D. Knezevic, L. Nguyen, and A. T. Patera, "Pde apps for acoustic ducts: A parametrized component-to-system model-order-reduction approach," in Numerical Mathematics and Advanced Applications ENUMATH 2017 (F. A. Radu, K. Kumar, I. Berre, J. M. Nordbotten, and I. S. Pop, eds.), (Cham), pp. 3–33, Springer International Publishing, 2019.
17. M. Barrault, Y. Maday, N. C. Nguyen, and A. T. Patera, "An 'empirical interpolation' method: application to efficient reduced-basis discretization of partial differential equations," C. R. Math. Acad. Sci. Paris, vol. 339, no. 9, pp. 667–672, 2004.
18. R. Mojgani and M. Balajewicz, "Lagrangian basis method for dimensionality reduction of convection dominated nonlinear flows," 2017.
19. N. Cagniart, Y. Maday, and B. Stamm, "Model order reduction for problems with large convection effects," in Contributions to partial differential equations and applications, pp. 131–150, Springer, 2019.
20. A. Manzoni, "An efficient computational framework for reduced basis approximation and $a\ posteriori$ error estimation of parametrized Navier-Stokes flows," ESAIM Math. Model. Numer. Anal., vol. 48, no. 4, pp. 1199–1226, 2014.
21. A. Quarteroni and G. Rozza, "Numerical solution of parametrized Navier-Stokes equations by reduced basis methods," Numer. Methods Partial Differential Equations, vol. 23, no. 4, pp. 923–948, 2007.
22. J. Baiges, R. Codina, and S. Idelsohn, "A domain decomposition strategy for reduced order models. Application to the incompressible Navier-Stokes equations," Comput. Methods Appl. Mech. Engrg., vol. 267, pp. 23–42, 2013.
23. D. Xiao, F. Fang, C. E. Heaney, I. M. Navon, and C. C. Pain, "A domain decomposition method for the non-intrusive reduced order modelling of fluid flow," Comput. Methods Appl. Mech. Engrg., vol. 354, pp. 307–330, 2019.
24. A. Ern and J.-L. Guermond, Theory and practice of finite elements, vol. 159 of Applied Mathematical Sciences. Springer-Verlag, New York, 2004.
25. A. Ern and J.-L. Guermond, Finite elements. II, vol. 73 of Texts in Applied Mathematics. Springer, Cham, [2021] ©2021. Galerkin approximation, elliptic and mixed PDEs.
26. K. Kean and M. Schneier, "Error analysis of supremizer pressure recovery for POD based reduced-order models of the time-dependent Navier-Stokes equations," SIAM J. Numer. Anal., vol. 58, no. 4, pp. 2235–2264, 2020.
27. M. D. Gunzburger, "Mathematical aspects of finite element methods for incompressible viscous flows," in Finite Elements (D. L. Dwoyer, M. Y. Hussaini, and R. G. Voigt, eds.), (New York, NY), pp. 124–150, Springer New York, 1988.
28. J. Förste, "Temam, r., navier-stokes equations: Amsterdam-new york. north-holland publishing company. 1977. xvi, 454 s., us $45.00. dfl. 125.00. (studies in mathematics and its applications 2)," ZAMM - Journal of Applied Mathematics and Mechanics / Zeitschrift für Angewandte Mathematik und Mechanik, vol. 59, no. 9, pp. 489–489, 1979.
29. S. V. Lototskii and B. L. Rozovskii, "Passive scalar equation in a turbulent incompressible gaussian velocity field," Russian Mathematical Surveys, vol. 59, pp. 297–312, apr 2004.
30. G. Caloz and J. Rappaz, "Numerical analysis for nonlinear and bifurcation problems," in Techniques of Scientific Computing (Part 2), vol. 5 of Handbook of Numerical Analysis, pp. 487–637, Elsevier, 1997.
31. D. R. Bland., Legendre Polynomials, pp. 61–77. Dordrecht: Springer Netherlands, 1961.
32. P. Drineas and M. W. Mahoney, "Randnla: randomized numerical linear algebra," Communications of the ACM, vol. 59, no. 6, pp. 80–90, 2016.
33. A. Buhr and K. Smetana, "Randomized local model order reduction," SIAM J. Sci. Comput., vol. 40, no. 4, pp. A2120–A2151, 2018.
34. K. Kunisch and S. Volkwein, "Galerkin proper orthogonal decomposition methods for parabolic problems," Numer. Math., vol. 90, no. 1, pp. 117–148, 2001.
35. M. Hinze and S. Volkwein, "Proper orthogonal decomposition surrogate models for nonlinear dynamical systems: Error estimates and suboptimal control," in Dimension Reduction of Large-Scale Systems (P. Benner, D. C. Sorensen, and V. Mehrmann, eds.), (Berlin, Heidelberg), pp. 261–306, Springer Berlin Heidelberg, 2005.
36. C. Himpe, T. Leibner, and S. Rave, "Hierarchical approximate proper orthogonal decomposition," SIAM J. Sci. Comput., vol. 40, no. 5, pp. A3267–A3292, 2018.
37. J. Ballani, D. Huynh, D. Knezevic, L. Nguyen, and A. Patera, "A component-based hybrid reduced basis/finite element method for solid mechanics with local nonlinearities," Computer Methods in Applied Mechanics and Engineering, vol. 329, pp. 498–531, 2018.
38. F. Hecht, "New development in freefem++," J. Numer. Math., vol. 20, no. 3-4, pp. 251–265, 2012.